BTIC FILE COPY

②

TECHNICAL REPORT BRL-TR-3167

BRL

AD-A229 127

COMPUTATIONAL FLUID DYNAMICS APPLICATION TO THE AERODYNAMICS OF SYMMETRIC SABOT DISCARD

MICHAEL J. NUSCA

DTIC
ELECTE
NOV 21 1990
S E
D

OCTOBER 1990

U.S. ARMY LABORATORY COMMAND

BALLISTIC RESEARCH LABORATORY
ABERDEEN PROVING GROUND, MARYLAND

90 11 19 202

NOTICES

REPORT DOCUMENTATION PAGE

Form Approved
OMB No. 0704-0188

Public reporting burden for this collection of information is estimated to average 1 hour per response, including the time for reviewing instructions, searching existing data sources, gathering and maintaining the data needed, and completing and reviewing the collection of information. Send comments regarding this burden estimate or any other aspect of this collection of information, including suggestions for reducing this burden, to Washington Headquarters Services, Directorate for Information Operations and Reports, 1215 Jefferson Davis Highway, Suite 1204, Arlington, VA 22202-4302, and to the Office of Management and Budget, Paperwork Reduction Project (0704-0188), Washington, DC 20503.

1. AGENCY USE ONLY (Leave blank)	2. REPORT DATE	3. REPORT TYPE AND DATES COVERED
	October 1990	Final, Sep 89 – Sep 90

4. TITLE AND SUBTITLE

Computational Fluid Dynamics Application to the Aerodynamics of Symmetric Sabot Discard

5. FUNDING NUMBERS

1L162618AH80

6. AUTHOR(S)

Michael J. Nusca

7. PERFORMING ORGANIZATION NAME(S) AND ADDRESS(ES)

8. PERFORMING ORGANIZATION REPORT NUMBER

9. SPONSORING / MONITORING AGENCY NAME(S) AND ADDRESS(ES)

Ballistic Research Laboratory
ATTN: SLCBR-DD-T
Aberdeen Proving Ground, MD 21005-5066

10. SPONSORING / MONITORING AGENCY REPORT NUMBER

BRL-TR-3167

11. SUPPLEMENTARY NOTES

12a. DISTRIBUTION / AVAILABILITY STATEMENT

Approved for public release; distribution is unlimited.

12b. DISTRIBUTION CODE

13. ABSTRACT (Maximum 200 words)

Computational fluid dynamics solutions of the three-dimensional Navier-Stokes equations have been applied to sabot discard aerodynamics for gun-launched, saboted, armor-piercing projectiles. The portion of the launch cycle which involves strong aerodynamic interference between the projectiles and discarding sabot components has been investigated. The complex system of shock/boundary-layer interactions between the projectile and sabot, during the discard sequence, has been numerically simulated. Three sabot components were located symmetrically at various positions near a cone-cylinder projectile. Computed and measured surface pressures for the projectile and sabot compare favorably for Mach number 4.5 and Reynolds number six million. Solutions for a flight Reynolds number of 89 million have been obtained as well. Computational solutions indicate the importance of three-dimensional, multi-body simulations and boundary layer modeling.

14. SUBJECT TERMS		15. NUMBER OF PAGES
Navier-Stokes Aerodynamics Sabot Kinetic Energy Projectiles Launch Dynamics		47
		16. PRICE CODE

17. SECURITY CLASSIFICATION OF REPORT	18. SECURITY CLASSIFICATION OF THIS PAGE	19. SECURITY CLASSIFICATION OF ABSTRACT	20. LIMITATION OF ABSTRACT
UNCLASSIFIED	UNCLASSIFIED	UNCLASSIFIED	SAR

NSN 7540-01-280-5500

Standard Form 298 (Rev 2-89)
Prescribed by ANSI Std Z39-18
298-102

INTENTIONALLY LEFT BLANK.

Acknowledgement

The author wishes to acknowledge Dr. E.M. Schmidt, Chief of the Fluid Physics Branch, Launch and Flight Division, US Army Ballistic Research Laboratory for his substantial support of this work.

Accession For	
NTIS GRA&I	☒
DTIC TAB	☐
Unannounced	☐
Justification	

By_____

Distribution/

Availability Codes	
Dist	Avail and/or Special
A-1	

INTENTIONALLY LEFT BLANK.

Table of Contents

INTENTIONALLY LEFT BLANK.

List of Figures

I. INTRODUCTION

Currently, the most widely utilized design for kinetic energy, antitank applications is the gun-launched, fin-stabilized, long-rod projectile (Figure 1). The cross-sectional diameter of the rod is smaller than the diameter of the gun bore. Fins span the area between the rod and the gun tube. Therefore, a properly designed sabot (or carrier) is required to reduce in-bore balloting of the projectile. Once free of the gun tube the sabot must be discarded in order to permit unconstrained, low-drag flight to the target. Figures 2 and 3 show a typical sabot discard. The sabot is divided into three or four components along axial planes. For smooth bore gun tubes, these components separate from the projectile under the action of elastic and aerodynamic loads. During separation both mechanical interference and gasdynamic forces can result in significant alteration of the projectile's trajectory and may lead to unacceptable loss of accuracy at the target.

Schmidt and Shear[1,2] have demonstrated that aerodynamic interference generated by the sabot components, or petals, can be a significant source of projectile launch disturbance. Perturbations to the projectile's trajectory are magnified by geometric asymmetry in the discard pattern and by extended periods during launch when the sabot components are in close proximity to the projectile. A detailed understanding of the three-dimensional shock/boundary-layer interference flowfield between the sabot and the projectile is not available.

Schmidt and Plostins[3,4] have conducted an extensive experimental program to investigate the aerodynamics of sabot discard. During these tests a projectile and three sabot components were sting-mounted in the NASA Langley Unitary Plan wind tunnel facility 4 x 4 ft test section. The model configuration included a stationary cone-cylinder projectile (without fins) at zero angle-of-attack and three 120° included-angle sabot components. The sabot components were located symmetrically around the projectile. Figures 4 thru 6 show photographs and a schematic of the wind tunnel model and associated nomenclature. The cylinder section of the projectile was 50.8mm in diameter; the projectile had a length-to-diameter ratio of 10.5 and a 30° included-angle conical nose. Fifty static pressure taps were positioned on the surface between the 120° planes of symmetry, with four taps on the conical section. The sabot had cylindrical inner and outer surfaces of radii 25.4 and 76.2mm, respectively, with the a leading edge chamfer of 40°. Fifty static pressure taps were located on the inner and outer surfaces. In order to test sabot petals at various positions near the projectile a single petal was mounted on a moveable sting. Since it was not practical to mount multiple actuated sabots splitter plates were attached to the projectile 120° apart as reflecting planes of symmetry (Figure 5). The splitter plates were 6.35mm thick and had a 15° leading edge chamfer. No pressure taps were used on the plates. The test Mach number and Reynolds number were 4.5 and 6.6 million per meter,

[1] Schmidt, E.M., and Shear, D.D., "Aerodynamic Interference During Sabot Discard," AIAA Journal of Spacecraft and Rockets, Vol. 15, No. 3, May-June 1978, pp. 162-167.

[2] Schmidt, E.M., and Shear, D.D., "Launch Dynamics of a Single Flechette Round," US Army Ballistic Research Laboratory, Aberdeen Proving Ground, MD, BRL Report No. 1810, Aug. 1975.

[3] Schmidt, E.M., "Wind-Tunnel Measurements of Sabot-Discard Aerodynamics," AIAA Journal of Spacecraft and Rockets, Vol. 18, No. 3, May-June 1981, pp. 235-240.

[4] Schmidt, E.M., and Plostins, P., "Aerodynamics of Asymmetric Sabot Discard," US Army Ballistic Research Laboratory, Aberdeen Proving Ground, MD, ARBRL-MR-03261, June 1983.

respectively. A typical flight Reynolds number of about 89 million per meter could not be reproduced in the tunnel; unfortunately, test results showed regions of shock/boundary-layer interaction, separated flow and other viscous phenomena. Figure 7 is a schematic of a portion of the test series. This "simulated sabot discard" sequence was executed for a single sabot petal and splitter plates on the projectile. It provides a reasonable basis for comparison of computed and measured surface pressures during discard.

Initial analytical work for sabot discard aerodynamics relied on the Newtonian flow approximation and empirical aerodynamic interaction analyses; for example the AVCO code.[5,6] These assumptions make discard computations tractable and in some cases represent accurate approximations. However, it is apparent that the multiple shock/expansion interaction flowfield between the projectile and sabot petals is an essential part of the analysis. The initial version of the AVCO code[5] evaluated the aerodynamic loadings on the sabot segments using Newtonian theory and a subsonic/supersonic inlet model; pressure forces on each surface of the segments, including sabot sides, were obtained separately and summed to provide results for total force and moments (excluding shear stress components). The code assumed that the aerodynamic coefficients for the projectile were known. Although the sabot separation process is initially dominated by aerodynamic interaction, the code assumed one-dimensional flow between the bodies. Recent versions[6] include an integrated flow element approach utilizing local shock/expansion procedures based on sabot surface pressures measured during wind tunnel tests.[3,4] These test data are used to determine pressure levels on certain sabot locations with linear variations assumed between these points. As a result, the code includes the effects of pressure pulses on the bodies caused by impinging and reflecting shock waves. When the sabot petals are not in close proximity to the projectile, Newtonian flow theory is used. In some cases, however, the code improvements produced overestimates of the discard process in contrast to initial code predictions. Consideration is limited to a general sabot configuration which is bounded radially by two cylindrical surfaces and axially by two conical surfaces.

This report describes computational fluid dynamics (CFD) solutions applied to the three-dimensional (3D) Navier-Stokes equations for symmetric sabot discard. During symmetric discard multiple sabot components are assumed to follow the same trajectory away from the projectile and the projectile is assumed to be at zero angle-of-attack. Figure 8 is an illustration of this configuration for three sabot petals. The computational domain for symmetric discard can be limited to a smaller portion of the entire flowfield around the configuration. Thus, requirements for three-dimensional simulations such as computational grid size, computer memory, and computer run time are reduced. For asymmetric discard the computational domain would be greatly expanded with a corresponding increase in computer requirements. The portion of the launch cycle which involves strong aerodynamic interference between the projectile and the sabot components is examined. Thus, simulations are performed for small vertical separation of the sabot petals and sabot angle of attack $\alpha \leq 18°$. Numerical simulations reported were performed for the wind tunnel model configuration illustrated in Figures 4 thru 6.

[5] Crimi. P., and Siegelman, D., "Analysis of Mechanical and Gasdynamic Loadings During Sabot Discard from Gun-Launched Projectiles," US Army Ballistic Research Laboratory, Aberdeen Proving Ground, MD, ARBRL-CR-341, June 1977.

[6] Siegelman. D., Wang, J., and Crimi, P., "Computation of Sabot Discard," US Army Ballistic Research Laboratory, Aberdeen Proving Ground, MD, ARBRL-CR-505, Feb. 1983.

II. COMPUTATIONAL APPROACH

The CFD approach described in this section can be used to predict the compressible flowfield around single and multiple component non-axisymmetric projectiles by solving the Reynolds-averaged 3D Navier-Stokes equations. The USA-PG3 code was developed by Chakravarthy.[7,8] The Navier-Stokes equations are written using the perfect gas assumption, however versions of the code for a real gas (e.g. equilibrium air, non-equilibrium gas and reacting flow) have been documented as well.[9,10] Both laminar and turbulent flows can be investigated, thus, a turbulence model[11] is required for closure. In addition, backflow regions can be present, thus, a backflow turbulence model[12] is included. The equations are transformed into conservation law form and discretized using finite volume approximations. The USA-PG3 code uses a class of numerical algorithms termed total variational diminishing (TVD) which do not require the inclusion of explicit smoothing or global dissipation functions to achieve numerical stability. The resulting set of equations is solved using an implicit, factored, time-stepping algorithm. The solution takes place on a computational grid that is generated around the projectile and sabot petals in zones. The zonal boundaries can be made transparent to the flowfield calculation. This code has been previously employed in the solution of subsonic, transonic, supersonic and mixed flow problems including complex three-dimensional and multi-body configurations by Chakravarthy et.al. [7,8,13-16]

1. EQUATIONS OF MOTION

The compressible, Reynolds-averaged Navier-Stokes (RANS) equations for 3D flow are written in the following conservation form. The dependent variables u, v, w and e are

[7] *Chakravarthy S.R., Szema K.Y., Goldberg U.C., Gorski J.J., and Osher S., "Application of a New Class of High Accuracy TVD Schemes to the Navier-Stokes Equations," AIAA-85-0165, Proceedings of the 23rd AIAA Aerospace Sciences Meeting, Reno NV., January 14-17, 1985.*

[8] *Chakravarthy S.R., Szema K.Y., and Haney, J.W., "Unified Nose-to-Tail Computational Method for Hypersonic Vehicle Applications," AIAA-88-2564, Proceedings of the 6th AIAA Applied Aerodynamics Conference, Williamsburg, VA, June 6-8, 1988.*

[9] *Ota, D.K., Chakravarthy S.R., and Darling, J.C., "An Equilibrium Air Navier-Stokes Code for Hypersonic Flows," AIAA-88-0419, Proceedings of the 26th AIAA Aerospace Sciences Meeting, Reno NV., January 11-14, 1988.*

[10] *Palaniswamy, S., and Chakravarthy, S.R., "Finite Rate Chemistry for USA Series Codes: Formulation and Applications," AIAA-89-0200, Proceedings of the 27th AIAA Aerospace Sciences Meeting, Reno, NV, January 9-12, 1989.*

[11] *Baldwin, B.S. and Lomax, H., "Thin Layer Approximation and Algebraic Model for Separated Turbulent Flows," AIAA-78-257, Proceedings of the 16th AIAA Aerospace Sciences Meeting, Huntsville, AL, January 16-18, 1978.*

[12] *Goldberg U.C., "Separated Flow Treatment with a New Turbulence Model," AIAA Journal, Vol. 24, No. 10, October 1986, pp. 1711-1713.*

[13] *Szema, K.Y., Chakravarthy S.R., Riba, W.T., Byerly, J., and Dresser, H.S., "Multi-Zone Euler Marching Technique for Flow Over Single and Multi-Body Configurations," AIAA-87-0592, Proceedings of the 25th AIAA Aerospace Sciences Meeting, Reno NV, January 12-15, 1987.*

[14] *Szema, K.Y., Chakravarthy S.R., Pan, D., Bihari, B.L., Riba, W.T., Akdag, V.M., and Dresser, H.S., "The Application of a Unified Marching Technique for Flow Over Complex 3-Dimensional Configurations Across the Mach Number Range," AIAA-88-0276, Proceedings of the 26th AIAA Aerospace Sciences Meeting, Reno NV, January 11-14, 1988.*

[15] *Chen, C.L., Ramakrishnan, S., Szema, K.Y., Dresser, H.S., and Rajagopal, K., "Multi-Zonal Navier-Stokes Solutions for the Multi-Body Space Shuttle Configuration," AIAA-90-0434, Proceedings of the 28th AIAA Aerospace Sciences Meeting, Reno NV. January 8-11, 1990.*

[16] *Nusca, M.J., Chakravarthy, S.R., and Goldberg, U.C., "Computational Fluid Dynamics Capability for the Solid-Fuel Ramjet Projectile," AIAA Journal of Propulsion and Power, Vol. 6, No. 3, May-June 1990, pp. 256-262.*

mass-averaged.

$$\frac{\partial W}{\partial t} + \frac{\partial F}{\partial x} + \frac{\partial G}{\partial y} + \frac{\partial H}{\partial z} = 0 \tag{1}$$

$$W = \begin{pmatrix} \rho \\ \rho u \\ \rho v \\ \rho w \\ \rho e \end{pmatrix}, \; F = \begin{pmatrix} \rho u \\ \rho u^2 - \sigma_{xx} \\ \rho u v - \tau_{xy} \\ \rho u w - \tau_{xz} \\ \rho u e + \dot{q}_x - \sigma_{xx} u - \tau_{xy} v - \tau_{xz} w \end{pmatrix}$$

$$G = \begin{pmatrix} \rho v \\ \rho v u - \tau_{yx} \\ \rho v^2 - \sigma_{yy} \\ \rho v w - \tau_{yz} \\ \rho v e + \dot{q}_y - \tau_{yx} u - \sigma_{yy} v - \tau_{yz} w \end{pmatrix}, \; H = \begin{pmatrix} \rho w \\ \rho w u - \tau_{zx} \\ \rho w v - \tau_{zy} \\ \rho w^2 - \sigma_{zz} \\ \rho w e + \dot{q}_z - \tau_{zx} u - \tau_{zy} v - \sigma_{zz} w \end{pmatrix}$$

$$\sigma_{xx} = -p - \frac{2}{3}(\mu + \mu_t)\nabla \cdot U + 2(\mu + \mu_t)\frac{\partial u}{\partial x} \tag{2}$$

$$\sigma_{yy} = -p - \frac{2}{3}(\mu + \mu_t)\nabla \cdot U + 2(\mu + \mu_t)\frac{\partial v}{\partial y} \tag{3}$$

$$\sigma_{zz} = -p - \frac{2}{3}(\mu + \mu_t)\nabla \cdot U + 2(\mu + \mu_t)\frac{\partial w}{\partial z} \tag{4}$$

$$\tau_{xy} = \tau_{yx} = (\mu + \mu_t)\left(\frac{\partial u}{\partial y} + \frac{\partial v}{\partial x}\right) \tag{5}$$

$$\tau_{xz} = \tau_{zx} = (\mu + \mu_t)\left(\frac{\partial w}{\partial x} + \frac{\partial u}{\partial z}\right) \tag{6}$$

$$\tau_{yz} = \tau_{zy} = (\mu + \mu_t)\left(\frac{\partial v}{\partial z} + \frac{\partial w}{\partial y}\right) \tag{7}$$

$$\dot{q}_x = -c_p\left(\frac{\mu}{\text{Pr}} + \frac{\mu_t}{\text{Pr}_t}\right)\frac{\partial T}{\partial x} \tag{8}$$

$$\dot{q}_y = -c_p\left(\frac{\mu}{\text{Pr}} + \frac{\mu_t}{\text{Pr}_t}\right)\frac{\partial T}{\partial y} \tag{9}$$

$$\dot{q}_z = -c_p\left(\frac{\mu}{\text{Pr}} + \frac{\mu_t}{\text{Pr}_t}\right)\frac{\partial T}{\partial z} \tag{10}$$

$$e = c_v T + \frac{1}{2}(u^2 + v^2 + w^2) \tag{11}$$

In Equations 2-10 the laminar and eddy viscosities, μ and μ_t, are implicitly divided by the reference Reynolds number. The equations used for the Euler (inviscid) calculations are obtained from Equations 1-11 by setting both laminar and eddy viscosities to zero. In all calculations the flow medium (air) was assumed to be a perfect gas satisfying the equation of state:

$$p = \rho \Re T \tag{12}$$

The following power law was used to relate molecular viscosity to temperature [17]

$$\frac{\mu}{\mu_o} = \left(\frac{T}{T_o}\right)^n \tag{13}$$

where $\mu_o = 0.1716$ milliPoise, $T_o = 491.6$ R, and $n = 0.64874$. The laminar and turbulent Prandtl numbers, Pr and Pr_t, were assumed constant with values of 0.72 and 0.9 respectively. The ratio of specific heats, γ, was also assumed constant and equal to 1.4.

Assuming a time-invariant grid and using the transformation of coordinates implied by $\tau = t$, $\xi = \xi(x, y, z)$, $\eta = \eta(x, y, z)$ and $\zeta = \zeta(x, y, z)$, Equation 1 can be recast into conservation form where ξ, η and ζ are the new independent variables and x_ξ, x_η, x_ζ, y_ξ, y_η, y_ζ, z_ξ, z_η and z_ζ are the nine transformation coefficients obtained numerically from the mapping procedure. The transformed time variable is represented by τ.

2. TURBULENCE MODELING

The shock/boundary-layer interference flowfield between the projectile and sabot petals can include large regions of recirculating flow. Thus, modeling of these regions can be critical to the overall flowfield solution quality. However most existing turbulence models either do not treat such regions or do so in a semi-empirical fashion that is frequently inadequate. To improve the predictive capabili *f* separated flows using current Reynolds-averaged Navier-Stokes codes a new turbulence model has been recently developed.[12] The new turbulence model is based on experimental observations of detached flows. The model prescribes turbulence kinetic energy (k) and dissipation (ϵ) analytically within backflows. A Gaussian variation of k normal to wall surfaces is assumed. The length scale of turbulence is proportional to the local distance from the wall to the edge of the viscous sublayer which is located outside the backflow region. The latter feature is a basic assumption of the model. The stress scale is the local maximum Reynolds stress which typically occurs around the middle of the boundary layer well outside the separation bubble. This scale must be supplied by a turbulence model that is used beyond backflow regions.

The main equations of the backflow model are given in Reference 12. A formula for the eddy viscosity distribution within backflows is derived and used to supply eddy viscosity for the Reynolds-averaged equations when the calculations are done inside separation bubbles. Outside of them, another turbulence model (for example Baldwin-Lomax[11]) supplies the values of eddy viscosity. While the Baldwin-Lomax turbulence model is used to detect flow separation and to initiate application of the backflow model, the latter model can relocate the separation point. Comparisons of the Baldwin-Lomax turbulence model and Goldberg's backflow model are given in References 16 and 18. For further details of how the model treats the influence of large eddies residing outside detached regions, the history effect of these eddies downstream of reattachment, and the mutual influence of multiple walls on the eddy viscosity, see References 12 and 19.

---

[17] *Mazor, G., Ben-Dor, G. and Igra, O., "A Simple and Accurate Expression for the Viscosity of Nonpolar Diatomic Gases up to 10,000 K," AIAA Journal, Vol. 23, No. 4, April 1985, pp. 636-638.*

[18] *Goldberg, U.C., "Separated Flows Calculations With A New Turbulence Model," presented at the IACM First World Congress on Computational Mechanics, Austin, TX, Sept. 1986.*

[19] *Goldberg, U.C., "Prediction of Separated Flows With A New Turbulence Model," AIAA Journal, Vol. 26, No. 4, April*

3. COMPUTATIONAL ALGORITHM

The spatial discretization technique for the equations of motion must be reliable and robust if it is to successfully capture the complex physics of projectile/sabot interacting flowfields. The TVD formulation for the convective terms (the hyperbolic part of the time-dependent Navier-Stokes equations) along with a special treatment of the dissipative terms provides an appropriate simulation. Any conventional time discretization method suitable for the Navier-Stokes equations can be used together with this space discretization methodology; for example, approximate factorization and relaxation techniques. In recent years, TVD formulations have been constructed for shock-capturing finite-difference methods.[7,8] Near large gradients in the solution (extrema) TVD schemes automatically reduce to first-order accurate discretizations locally while away from extrema they can be constructed to be of higher-order accuracy. This local effect restricts the maximum global accuracy possible for TVD schemes to third order for steady-state solutions.

TVD methods manifest many properties desirable in numerical solution procedures. By design they avoid numerical oscillations and "expansion shocks" while at the same time being of higher-order accuracy; "expansion shocks" are shock waves which do not satisfy the entropy inequality. TVD formulations are also based on the principle of discrete or numerical conservation which is the numerical analog of physical conservation of mass, momentum, and energy. Thus, TVD schemes can "capture" discontinuities with high resolution. At a fundamental level they are based on upwind schemes; therefore, they closely simulate the signal propagation properties of hyperbolic equations. Schemes based on the TVD formulation are completely defined. In contrast, central difference schemes involve global dissipation terms for stability and have one or more coefficients that must be judiciously chosen to achieve desirable results.

Proper treatment of the dissipative terms of the Navier-Stokes equations is also important in the construction of reliable numerical methods. Unidirectional second derivative terms are treated by using central difference approximations. Cross derivatives are represented by finite-differences the nature of which depends upon the sign of the coefficient of such terms. This treatment augments diagonal dominance of the resulting set of discretized equations without detracting from the accuracy and while adding to the reliability of the numerical procedure. Further details can be found in References 7 and 8.

4. COMPUTATIONAL GRID

Numerical simulation of the interacting flowfield about projectile/sabot combinations is complicated by the non-axisymmetric geometry. For even simplified sabot configurations sharp corners severely hamper conventional grid generation schemes that require one set of grid lines to be tangential and another set to be normal to the surface. Projectile/sabot geometries are more easily gridded using the zonal approach. The configuration is divided into zones of simple geometric shape. In each zone an algebraic grid is generated with grid clustering near walls and high flow gradient regions. In the zonal approach, the computational method and computer program are constructed in such a manner that each

zone may be considered as an independent module interacting with other zones before or after the information corresponding to each zone is updated one cycle. In addition, the zonal boundaries can be made transparent to flowfield phenomena (e.g. shock waves).

Zone designations for a typical 6-zone grid used for computations described in this report are shown in Figures 9 and 10. The actual grid is shown in Figures 11 and 12. Grid zone 1 covers the projectile from nose to base, zone 2 covers the area between zone 1 and the inner surface of the sabot petal, zone 4 covers the area between the outer surface of the sabot petal and the uppermost extent of the computational domain, zones 5 and 6 cover the projectile and sabot base regions, respectively. Zones 1 thru 6, excluding zone 3, extend from $\phi = 0$ to $60°$ in the azimuthal direction. Grid zone 3 covers the area between the sabot petal and the azimuthal extent of the computational domain. The entire 6-zone grid consists of 300,000 nodes and requires 10 million words of memory on the US Army Ballistic Research Laboratory (BRL) CRAY-2 supercomputer. Grid clustering was used along all walls to resolve boundary layer profiles and near geometric discontinuities to resolve flow gradients. The same grid sizes can be used for cases where the sabot petal is pitched to an angle of $\leq 18°$ due to the use of a no-reflection boundary condition on the uppermost surface of the computational domain (zone 4). These grid dimensions are assumed to be sufficient for preliminary computational simulations where relatively short computer run time was required. Grid refinement studies are underway including the use of a Poisson solver[20] to smooth the initial algebraic grid.

III. RESULTS

This report presents numerical simulations for the wind tunnel projectile/sabot model. The freestream Mach number and Reynolds Number are 4.5 and 6.6 million per meter, respectively. Simulations for Mach number 4.5 and Reynolds number 89 million per meter are shown as well. Calculations are presented for inviscid, laminar and turbulent flow modeling. Converged solutions required about 6 CPU hours for inviscid flow and 18 to 20 CPU hours for laminar and turbulent solutions on the BRL CRAY-2 computer.

Figure 13 shows pressure contours for the forward part of the projectile/sabot configuration in the pitch plane; in this case the pitch plane cuts across the center of the sabot petal (see Figure 8). Three sabot petals are assumed (i.e. no splitter plates) with the sabot base aligned with the projectile base, $\Delta x/D = 0$, projectile surface and sabot inner surface vertically separated by $\Delta y/D = .75$, and the sabots at zero angle-of-attack. Three horizontal lines extending from $x/D = 0$ to 5.625 are zonal grid boundaries. Large flow gradients (e.g. shock waves) are indicated by clustering of pressure contour lines. An oblique shock is attached to the projectile nosetip and a normal shock is slightly detached from the leading edge of the sabot petal. Downstream of these shocks a complex system of interactions and reflections results. Flow expansion at the cone-cylinder junction ($x/D \simeq$ 2.1) is followed by a strong oblique shock on the projectile ($x/D \simeq 2.8$). Thus, a high pressure, low speed and perhaps recirculating flow region may be present on the projectile

---

[20] *Rajagopal, K., Lick, W., Szema, K., Ramakrishnan, S., and Chen, C., "A Versatile Multi-Zonal Gridding Technique for Complex Geometries," AIAA-90-0011, Proceedings of the 28th AIAA Aerospace Sciences Meeting, Reno NV, January 8-11, 1990.*

at this location. This region terminates with a sonic throat condition ($x/D \simeq 4.22$) and a corresponding expansion to supersonic flow downstream.

Figure 14 shows the sonic ($M = 1$) Mach contours for the same configuration. Three horizontal lines extending from $x/D = 0$ to 5.625 are zonal grid boundaries. These contours indicate that a region of subsonic ($M < 1$) flow extends from $x/D \simeq 2.8$ to 4.22, between the sabot petal and the projectile.

Figure 15 shows the measured[3] and computed pressure distributions over the projectile and sabot surfaces in the pitch plane. Laminar flow modeling was employed. Computed pressures on the projectile surface agree favorably with the magnitude and location of a measured pressure peak ($x/D \simeq 4.22$) as well as an elevated pressure (low speed flow) region preceding this peak, $2 \leq x/D \leq 4.22$. The location of this pressure peak corresponds to the termination of a low speed flow region on the projectile (see remarks for Figure 14). Downstream of the pressure peak the agreement between computation and measurement is also favorable. On the inner surface of the sabot petal numerical simulation adequately predicts the pressure level and trend on the sabot slant surface, $2.75 \leq x/D \leq 3.94$. Pressure levels on the rest of the sabot section agree with measurements including a pressure rise at $x/D \simeq 5.5$. The computed magnitude of this rise is somewhat larger than observed.

Figure 16 shows the measured[3] and computed pressure distributions over the projectile surface for three azimuthal planes including the pitch plane, $\phi = 0°, 30°, 45°$. Laminar flow modeling was employed. Data indicate that the pressure peak at $x/D \simeq 4.22$ decreases in magnitude with increasing azimuthal angle. The three-dimensionality of the flowfield is also indicated by the numerical simulations; however, only the trend of the pressure drop is reproduced. Computations with grid clustering at the location of the pressure peak and/or turbulence modeling may improve the results.

Figures 17 and 18 show pressure distributions over the projectile and sabot surfaces in the pitch plane using inviscid, laminar and turbulent flow modeling. Neither laminar nor turbulent modeling conclusively provides the best overall agreement with data. Inviscid flow simulations require significantly less computer time by excluding the viscous terms in the Navier-Stokes equations. However, the inviscid simulation predicts a smaller magnitude pressure peak and lower pressures preceding the peak; this indicates these are perhaps viscous phenomena. The turbulent prediction agrees more favorably with the pressure levels forward and behind the pressure peak but underpredicts the magnitude of the peak. In particular pressures between the projectile and sabot, $x/D \geq 5$, are best reproduced by the turbulent calculation. In Figure 18 the inviscid simulation overpredicts sabot leading edge pressure and underpredicts pressure on the sabot slant surface ($2.75 \leq x/D \leq 3.94$). Only slight differences are noted between laminar and turbulent predictions of pressure on the sabot surface. Further investigation of laminar and turbulent flow modeling should be conducted using grids of finer spacing.

Calculations for the wind tunnel model with splitter plates attached to the projectile and a single sabot petal are presented in Figures 19, 20, and 21. Recall that the plates were included to provide reflecting planes of symmetry, 120° apart, when physical restraints did not allow the mounting of all three sabot petals. With the exception of these plates the projectile/sabot configuration was identical to that represented in the previous figures. The

8

same grid was employed with a no-slip flow boundary condition specified on the splitter plates. Since the grid was not clustered normal to the plate (see Figure 12) boundary layer growth was not adequately simulated on this wall. Laminar flow modeling was employed.

Figure 19 shows the pressure contours for the forward part of the configuration in the pitch plane and may be compared to Figure 13. The presence of splitter plates has altered the flowfield: in particular the normal shock on the sabot leading edge merges with a shock apparently originating from the plate leading edge to form a shock structure that is significantly different from the displayed in Figure 13. Figure 20 shows the pressure distributions for the projectile and sabot inner surfaces and may be compared to Figure 15. Data indicate that the magnitude of the pressure peak has decreased significantly for the configuration with splitter plates. Computed pressures accurately reproduce this effect. Computed pressures preceding the peak are not adequately predicted: this may be the result of laminar flow modeling or course normal grid spacing on the plate. Pressures on the sabot surface agree well with the measured data. Further investigation into the use of splitter plates is warranted since these plates significantly alter the computed flowfield while no such shock structure was evident in the wind tunnel tests.

Figure 21 shows the pressure distribution on the projectile and sabot surfaces in the pitch plane. The projectile/splitter plate configuration and one sabot petal was used. In this case the projectile surface and sabot inner surface are vertically separated by $\Delta y/D = .25$ and the sabot petal is at 4° angle-of-attack with respect to the projectile. Laminar flow modeling was employed. The pressure magnitudes and trends are similar to those of Figure 20 except for elevated pressures from $x/D = 7$ to 11 where the bodies are in closer proximity. The numerical simulation reproduces these higher pressures.

Calculations for an axisymmetric projectile/sabot configuration are presented in Figures 22 and 23. The axisymmetric configuration is generated by joining three sabot petals into a tube that is concentric with the projectile. In this case the vertical separation between the projectile surface and the inner tube surface is $\Delta y/D = .75$. This configuration was not tested in the wind tunnel, but is used to numerically investigate the applicability of two-dimensional simulations. Since the axisymmetric configuration does not require a 3D simulation the required computer time is reduced from 18 hours to 3 hours on the BRL CRAY-2. Figure 22 shows the pressure contours for the forward part of the configuration illustrating that the axisymmetric geometry generates a normal shock significantly detached from the sabot, or tube. As a result, this shock interferes with the flowfield at the cone-cylinder junction on the projectile, $x/D \simeq 2.1$. A strong oblique shock is generated on the projectile at this location. Figure 22 may be compared to pressure contours for the 3D geometry show in Figure 13. The axisymmetric flowfield is significantly different from that of the actual geometry: thus, the less expensive computation does not provide an adequate simulation.

Figure 23 shows the computed pressure distributions over the projectile and sabot surfaces for the axisymmetric configuration and the measured pressures for the actual geometry. Several pressure peaks are generated on the projectile surface. The pressure measurements on the sabot slant surface ($2.75 \leq x/D \leq 3.94$) are reproduced by the calculation, however pressures between the sabot (tube) and the projectile ($x/D \geq 4$) are much higher than measurements. These results indicate that the axisymmetric simulation pre-

dicts a choked flow between the projectile and the sabot and is not an adequate substitute for the non-axisymmetric simulation.

Figure 24 shows the computed pressure distribution over the projectile surface for turbulent flow and Reynolds number values of 6.6 million and 89 million. The three dimensional configuration was used with $\Delta x/D = 0$, $\Delta y/D = .75$, $\alpha = 0$, and three sabot petals (i.e. no splitter plates). Grid stretching was refined in the wall-normal direction so that 6 to 8 points define the boundary layer profile for both Re cases. Some differences are noted between the curves, most noteably a decrease in the magnitude of the peak pressure. The Re 89 million result approaches the inviscid result as shown in Figure 17. Pressure magnitudes and trends on the sabot inner surface were not noticeably effected by the increase in Reynolds number.

IV.   CONCLUSIONS

Computational fluid dynamics (CFD) solutions of the three-dimensional Navier-Stokes equations have been applied to the aerodynamics of symmetric sabot discard. The portion of the launch cycle which involves strong aerodynamic interference between the projectile and the sabot components has been examined. A configuration was considered that included a cone-cylinder projectile at zero angle-of-attack with three sabot components. Computed and measured projectile and sabot surface pressures are in good agreement for a freestream Mach number of 4.5 and wind tunnel Reynolds number of six million. Grid refinement studies are being pursued to improve agreement with data for some flow details. Computational modeling revealed the source of a measured pressure peak on the projectile surface as the termination of a region of high pressure, low speed flow. Computational solutions demonstrate the importance of three-dimensional, non-axisymmetric simulations over axisymmetric approximations, and viscous/turbulent flow modeling over the inviscid assumption. Pressure distributions on the projectile surface were found to be sensitive to freestream Reynolds number.

V.   FUTURE WORK

CFD methods proven using wind tunnel configurations are being applied to fielded projectile/sabot configurations with more complex sabot geometries. A technique for the integration of surface pressures and shear stress is being used to determine the aerodynamic forces and moments acting on the sabot surfaces. This output could be used in quasi-steady mode to supply aerodynamic inputs to a six degree-of-freedom sabot trajectory simulation. In addition, detailed 3D numerical computations are being used to enhance the engineering sabot design/analysis codes that are based on local shock-expansion gasdynamic techniques.
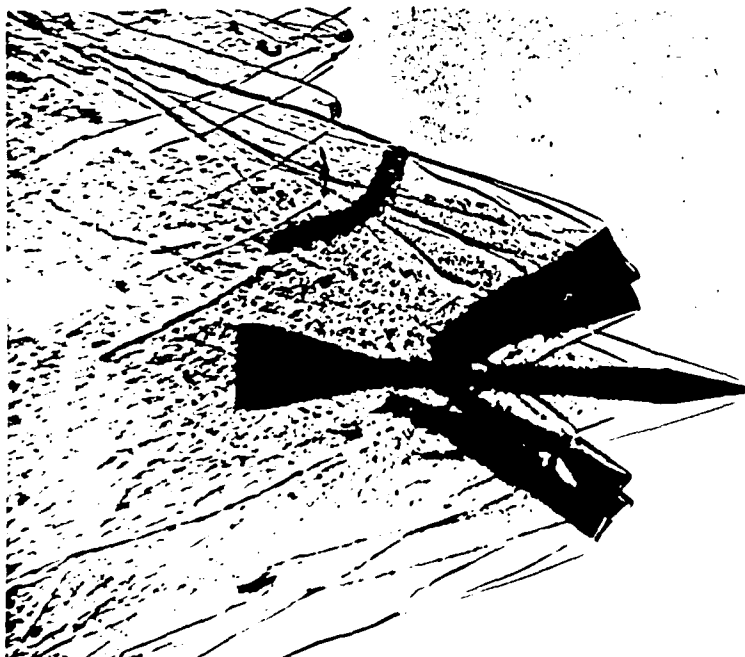
INTENTIONALLY LEFT BLANK.
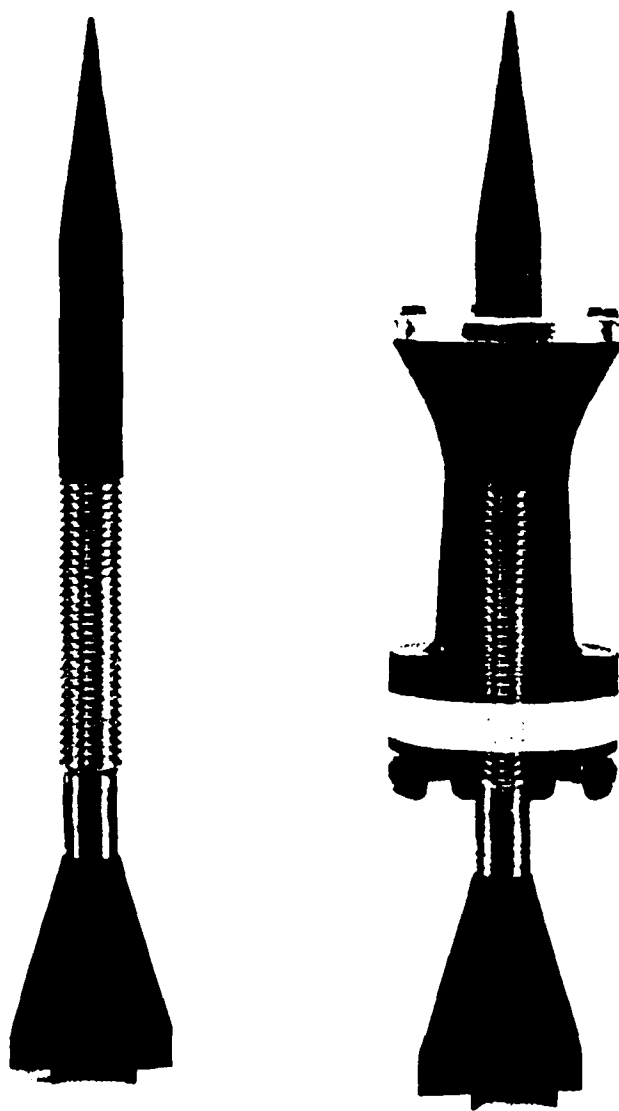
Figure 1. Typical kinetic energy long-rod projectiles with and without sabot (sabot shown in cutaway view).
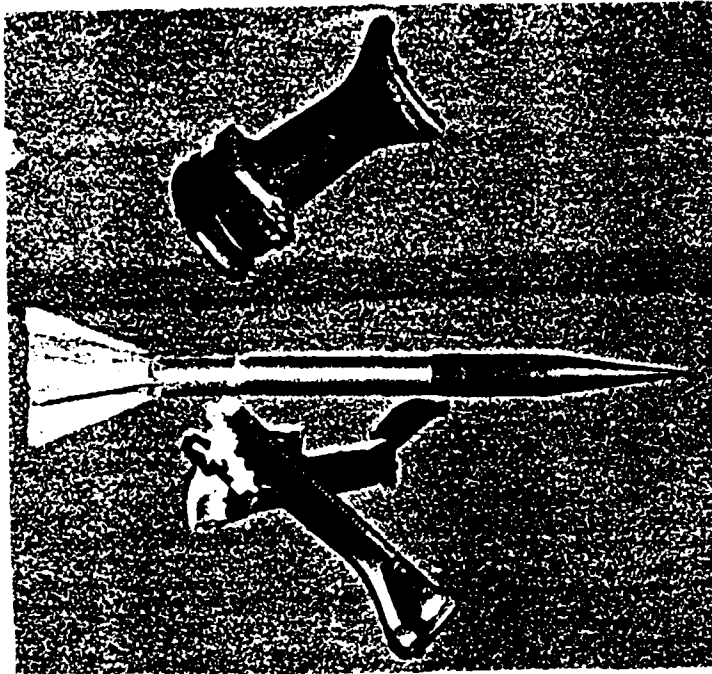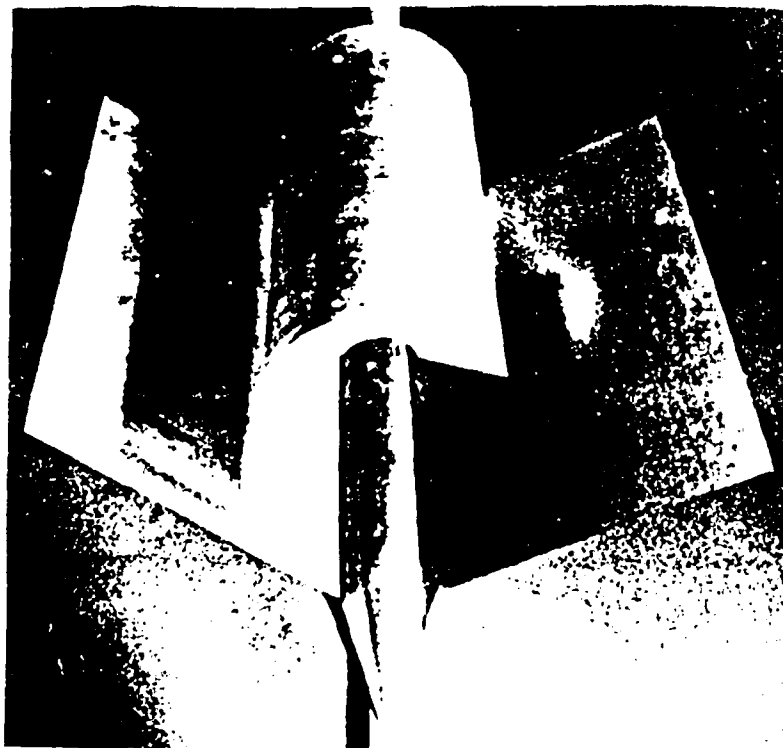
Figure 2. Photograph of typical kinetic energy long-rod projectile in free flight during three-petal sabot discard.

Figure 3. Shadowgraph of typical kinetic energy long-rod projectile in free flight during four-petal sabot discard.
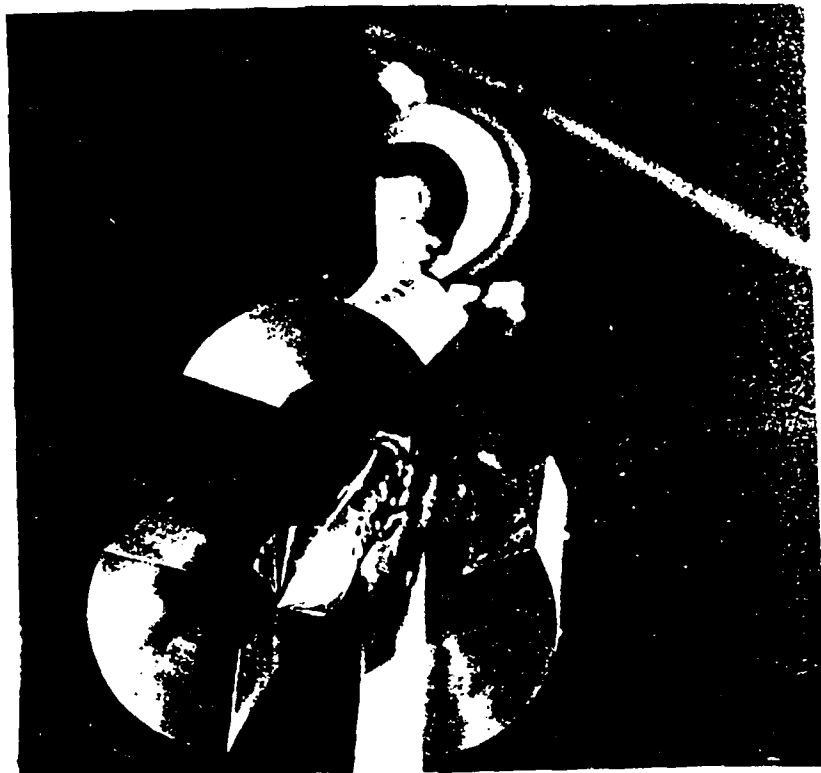
Figure 4. Photograph (front-view) of sting-mounted wind tunnel models showing cone-cylinder projectile (center) and three sabots.

Figure 5. Photograph (top-view) of sting-mounted wind tunnel models showing cone-cylinder projectile with splitter plates below one sabot component.
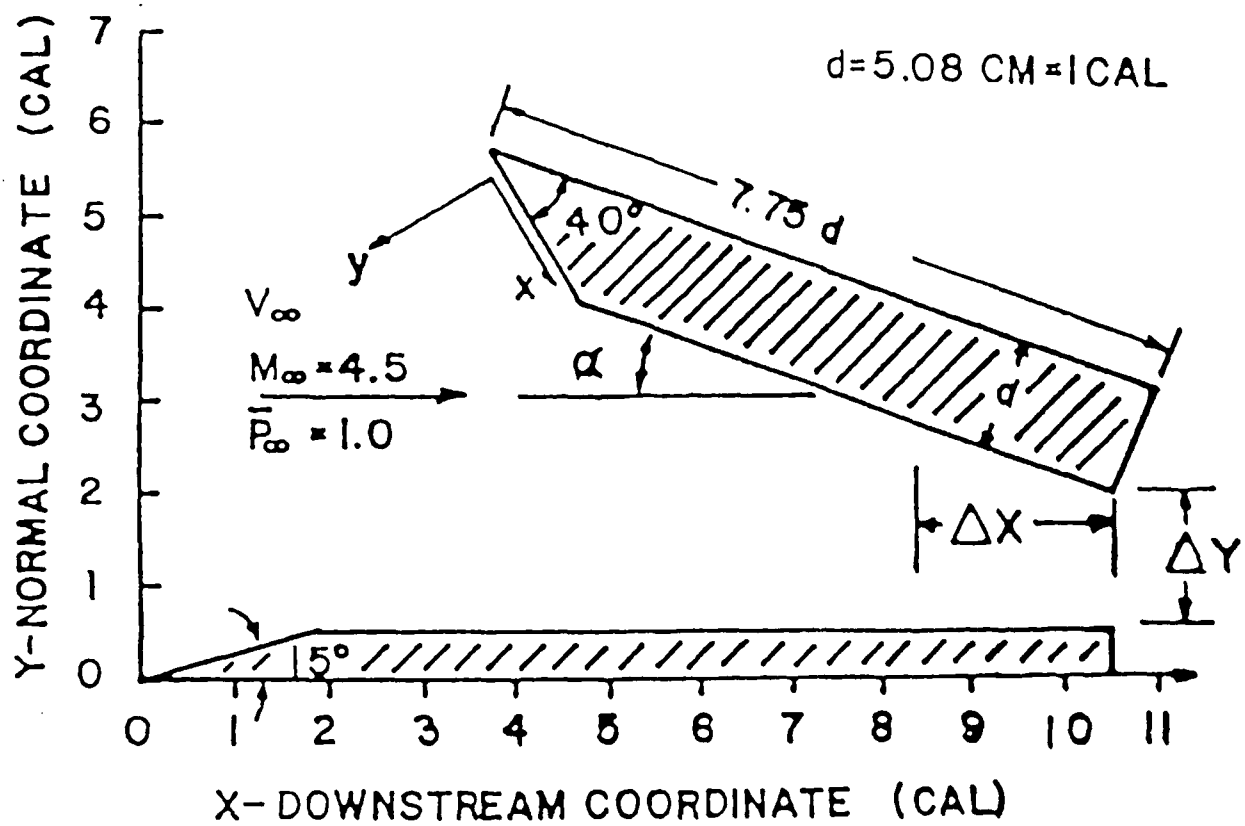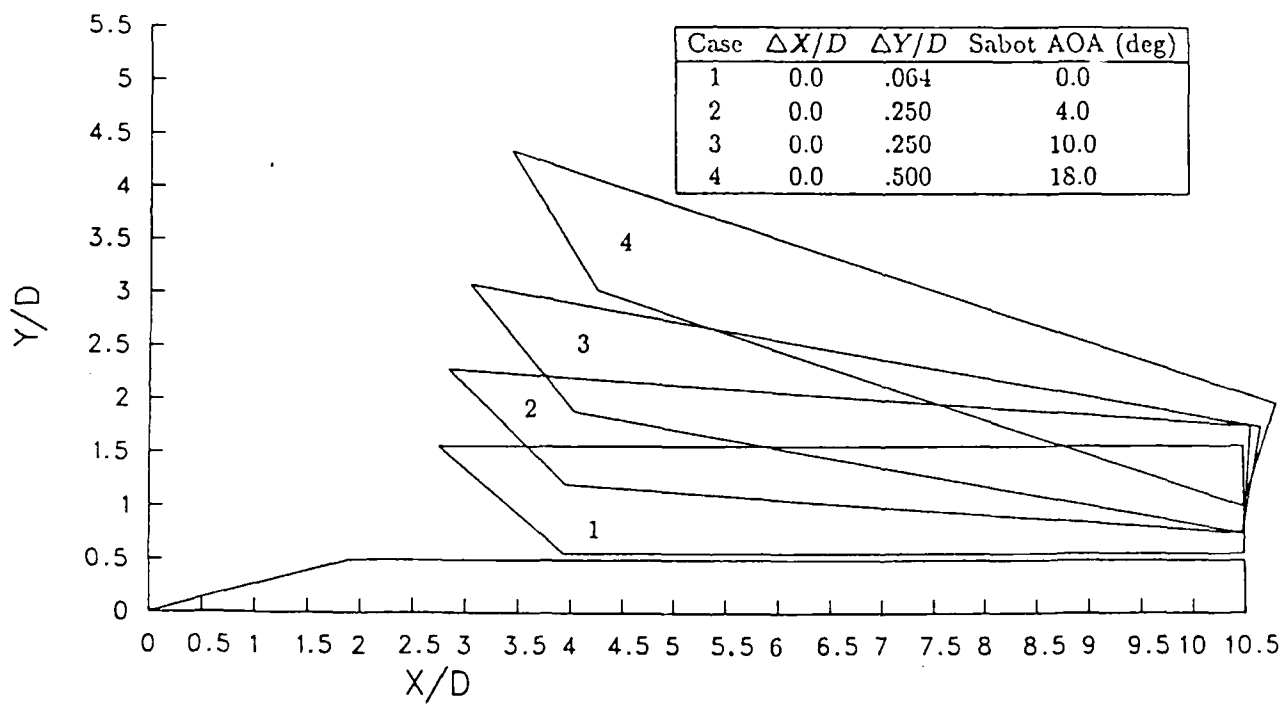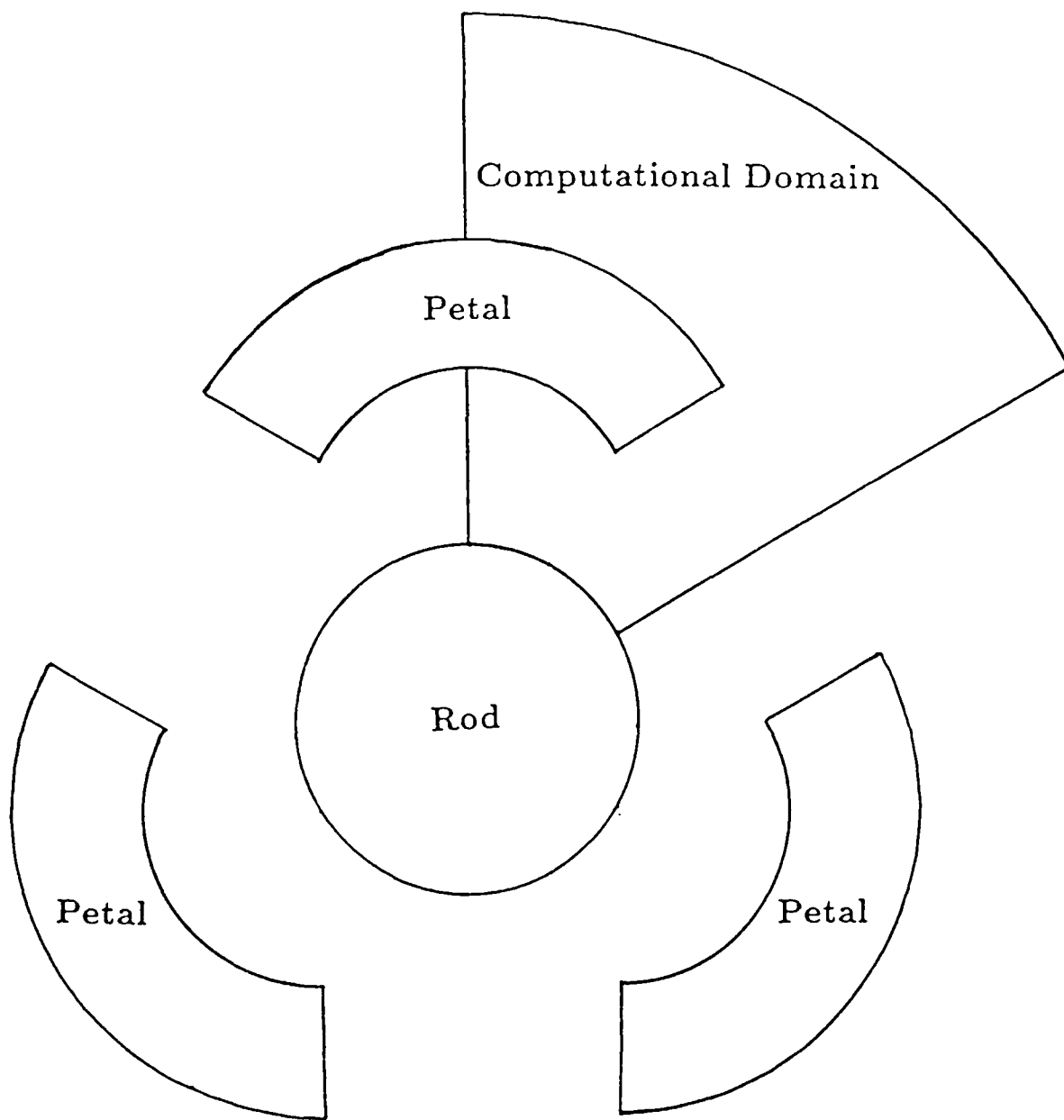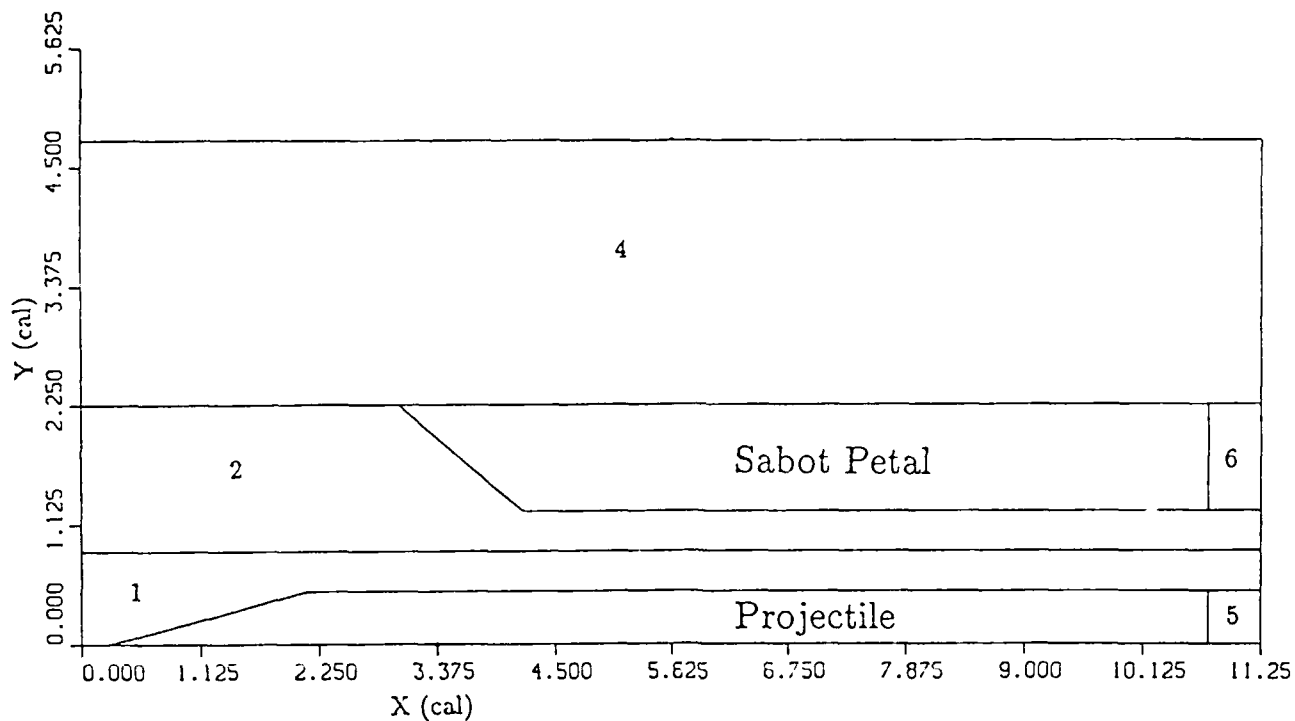
Figure 6. Schematic of wind tunnel model in the pitch plane ($\phi = 0, 180°$).

15

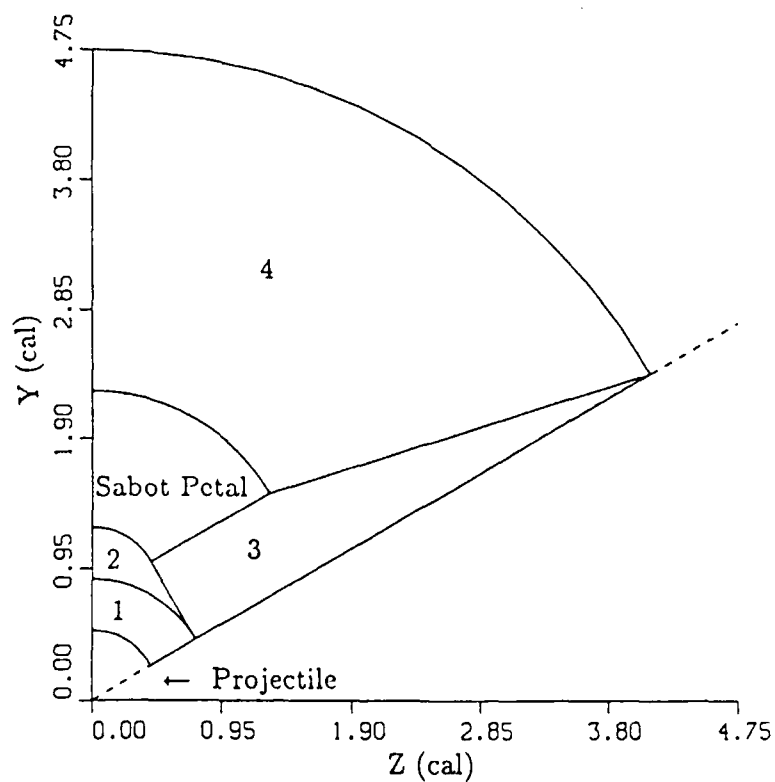| Case	$\Delta X/D$	$\Delta Y/D$	Sabot AOA (deg)
1	0.0	.064	0.0
2	0.0	.250	4.0
3	0.0	.250	10.0
4	0.0	.500	18.0

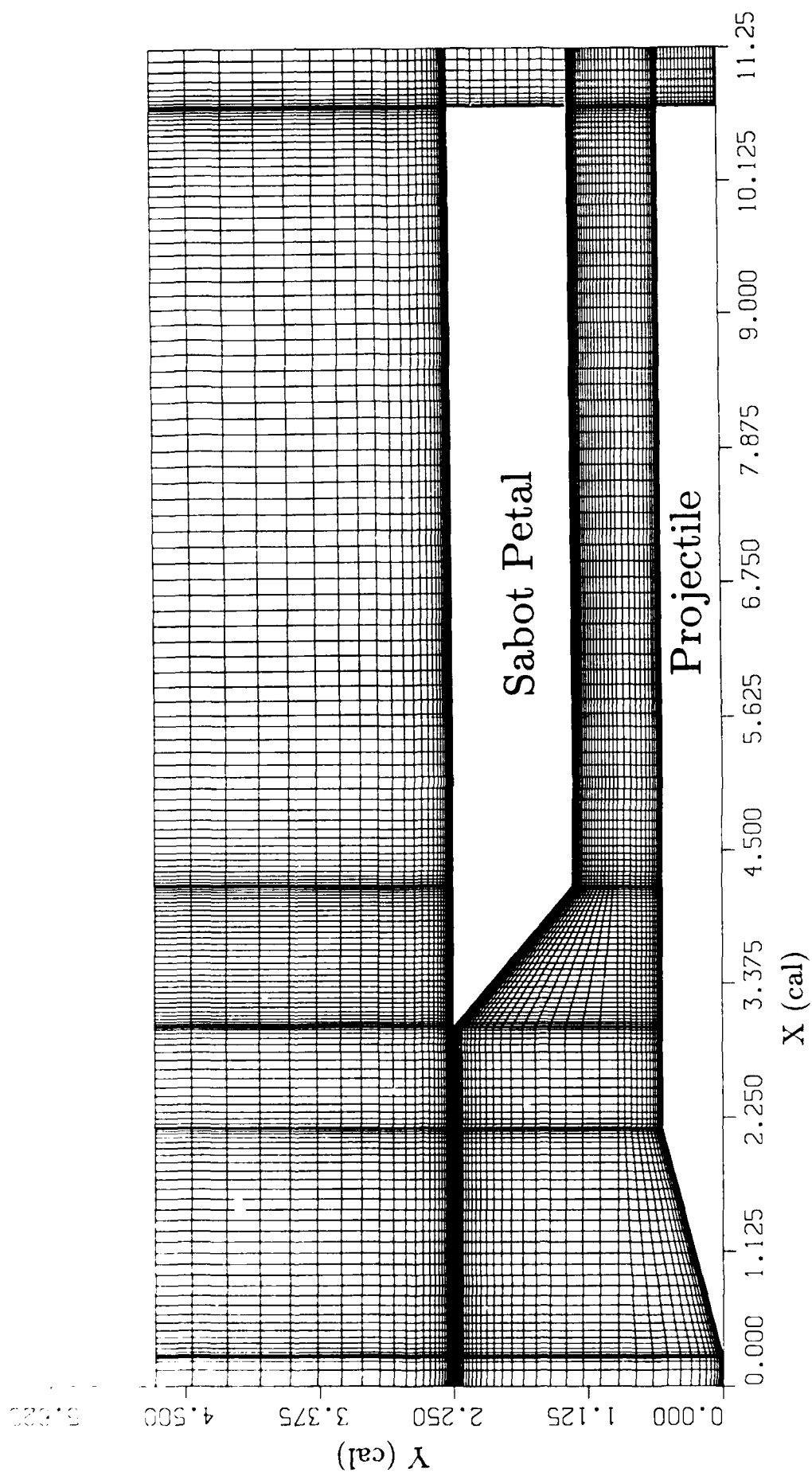**Figure 7.** Schematic of simulated sabot discard test sequence.

Figure 8. Schematic of symmetric sabot discard (rear-view) showing computational domain.
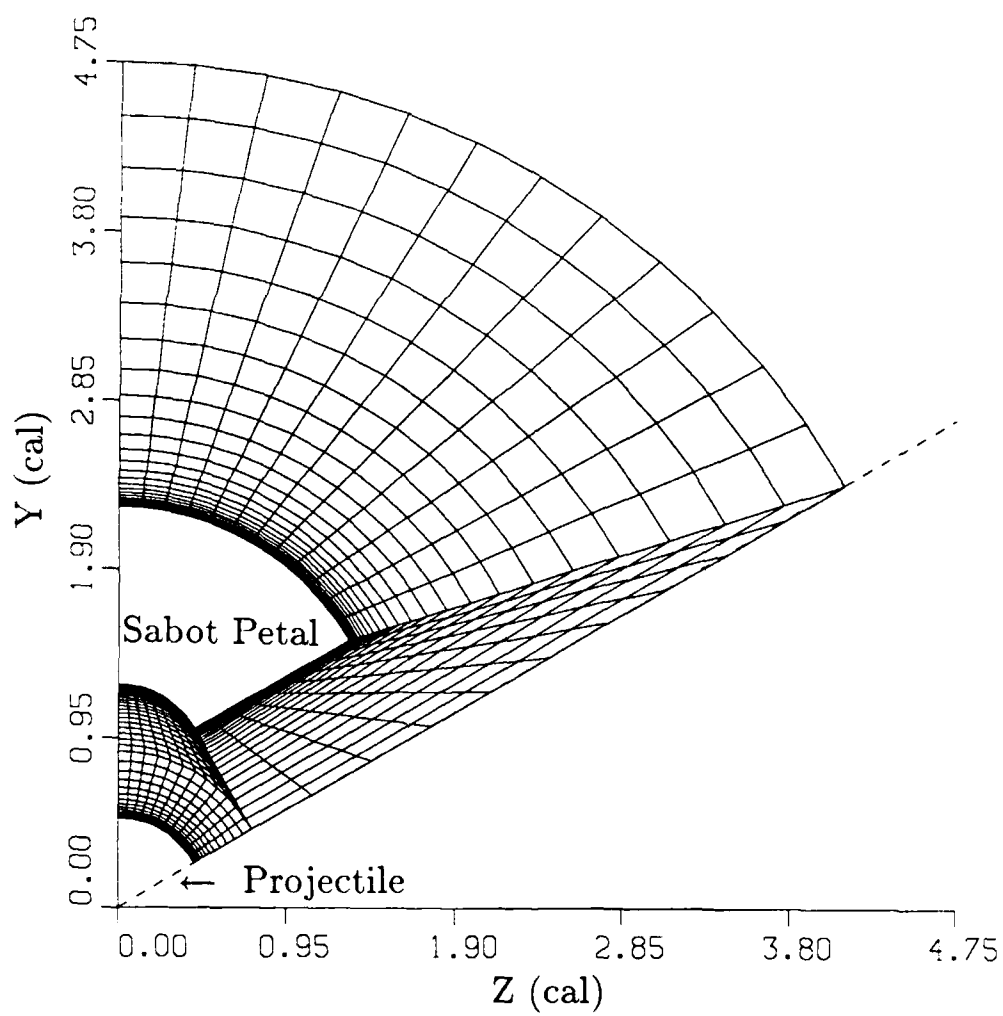
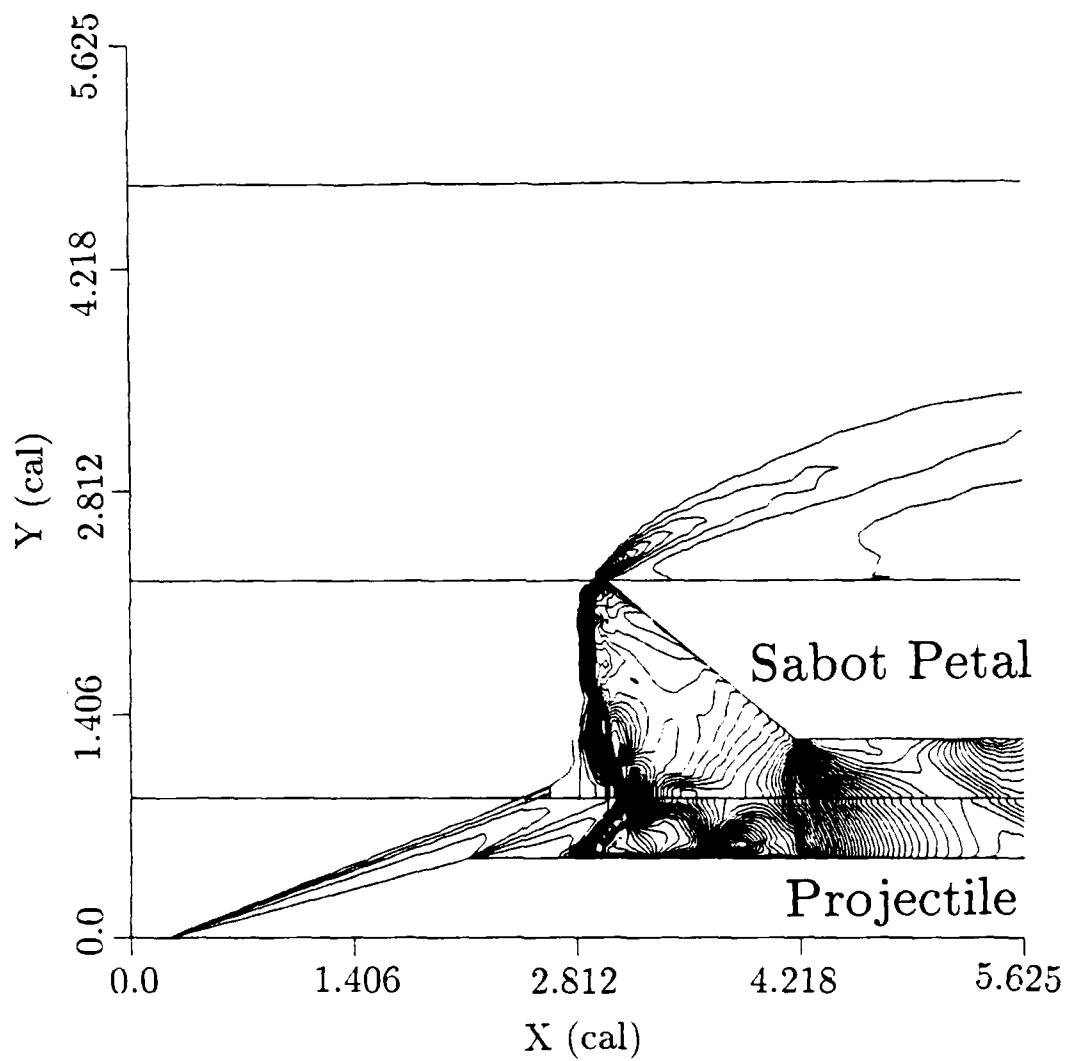**Figure 9.** Zone designations for projectile/sabot configuration in the pitch plane ($\phi = 0, 180°$).

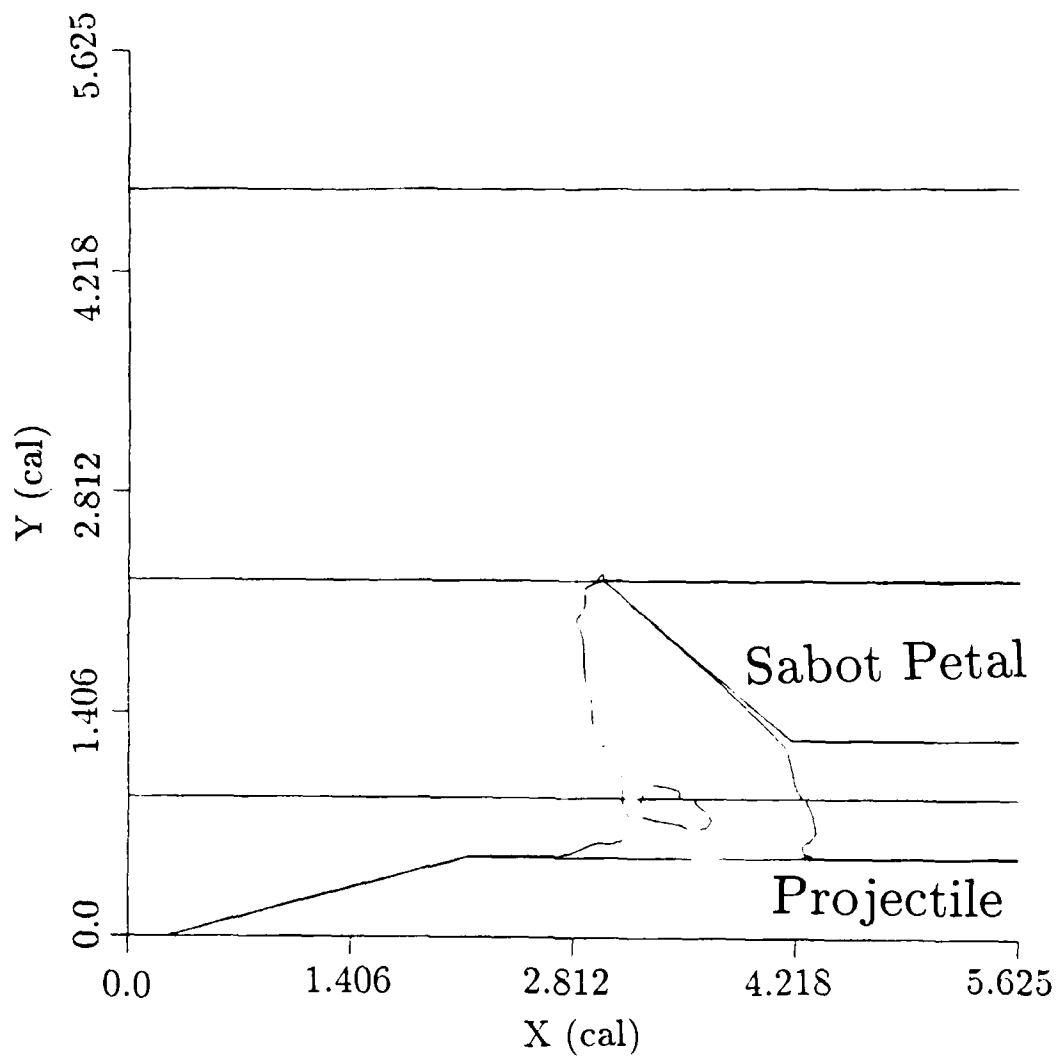**Figure 10.** Zone designations for projectile/sabot configuration in an axial plane.

Figure 11. Zonal computational grid in the pitch plane ($\phi = 0, 180^\circ$) for $\Delta r/D = 0$, $\Delta y/D = .75$, $\alpha = 0^\circ$.

Figure 12. Zonal grid in an axial ($x/D = 10$) plane for $\triangle x/D = 0$, $\triangle y/D = .75$, $\alpha = 0^\circ$.

20
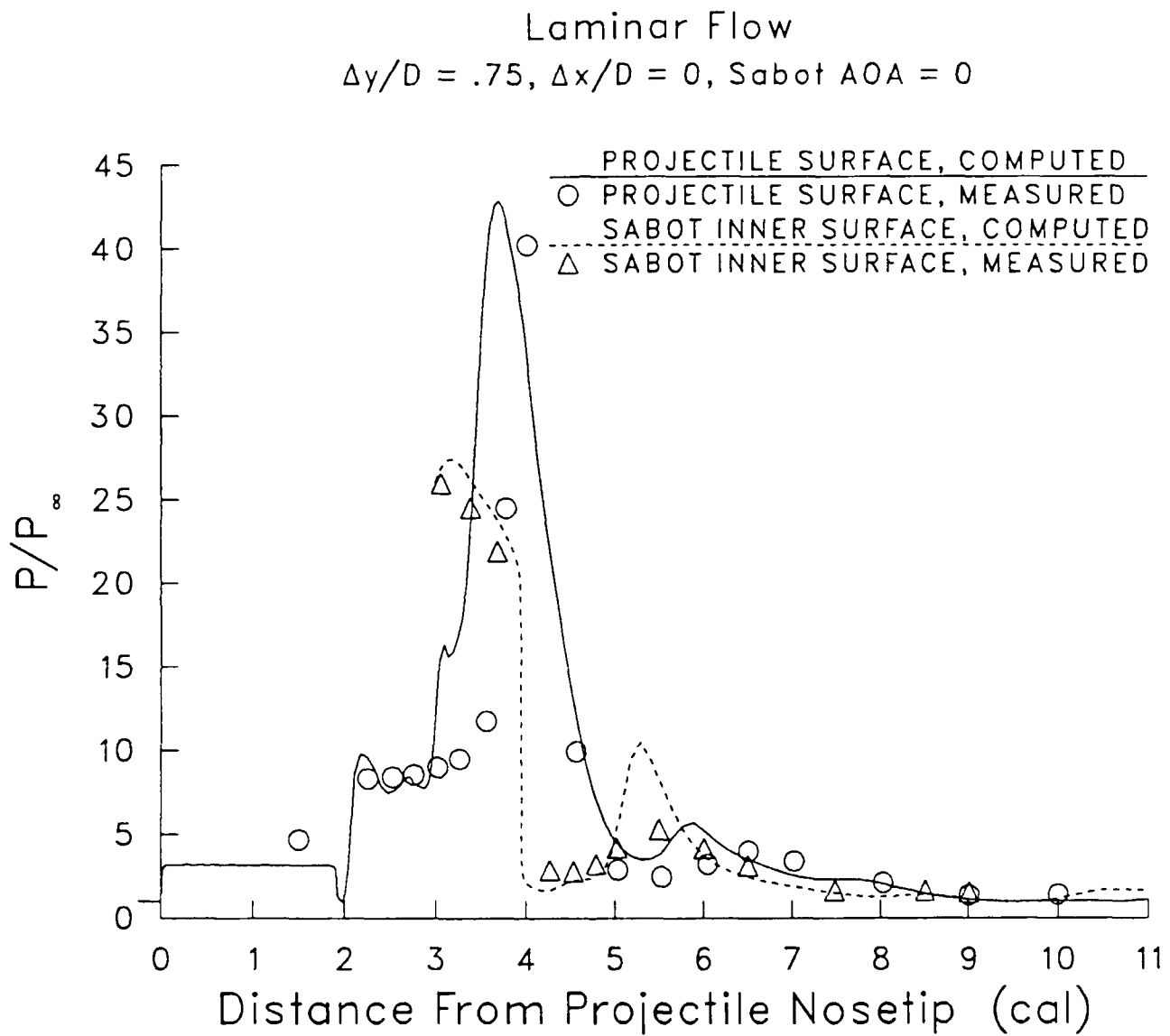
Figure 13. Laminar flow pressure contours in the pitch plane ($\phi = 0, 180°$) for $\triangle x/D = 0$, $\triangle y/D = .75$, $\alpha = 0°$.

Figure 14. Laminar flow sonic ($M = 1$) Mach contours in the pitch plane ($\phi = 0, 180°$) for $\triangle x/D = 0$, $\triangle y/D = .75$, $\alpha = 0°$.

Figure 15. Laminar flow pressure distributions on projectile and sabot surfaces in the pitch plane ($\phi = 0, 180°$) for $\triangle x/D = 0$, $\triangle y/D = .75$, $\alpha = 0°$.
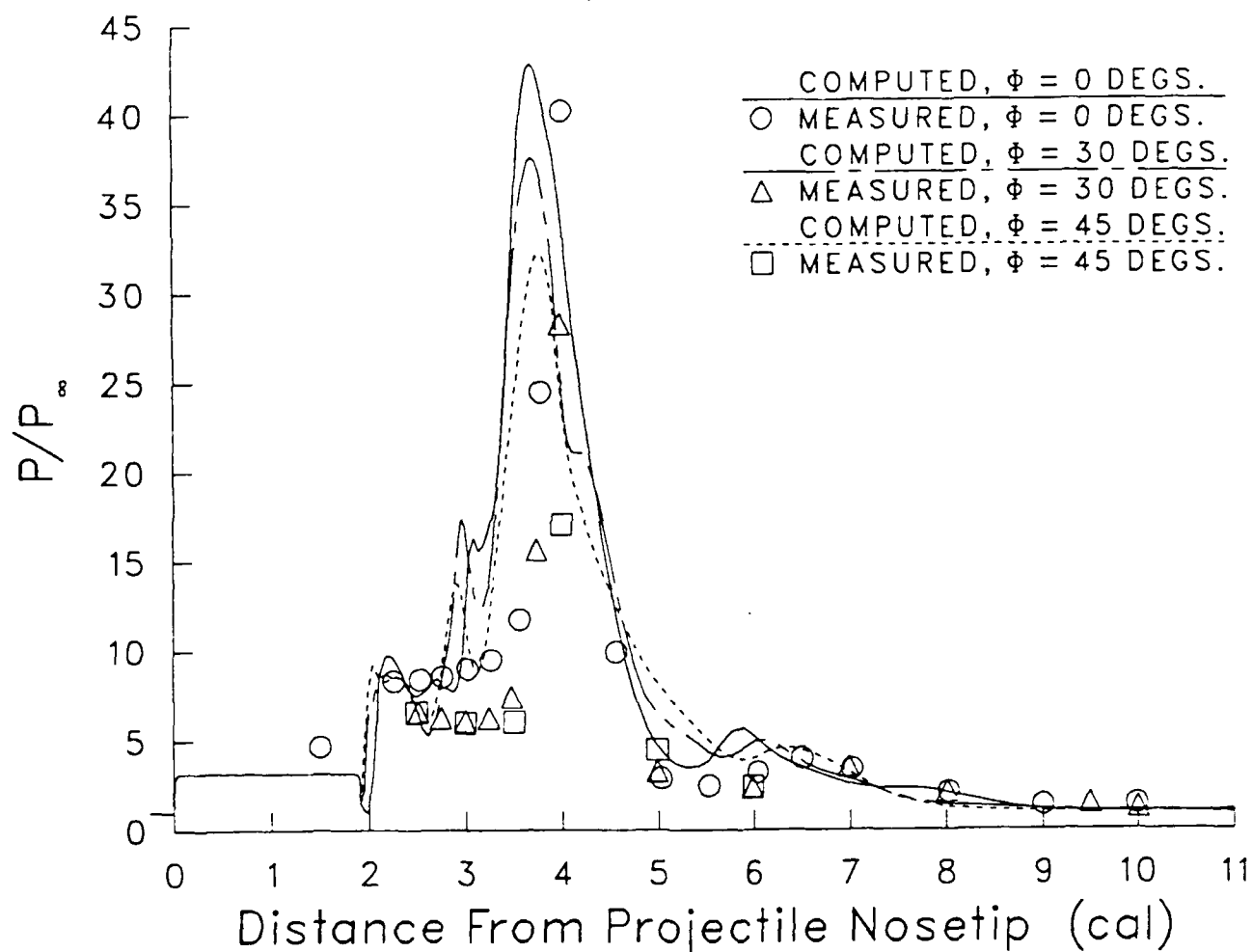
Figure 16. Laminar flow pressure distributions on projectile surface in the $\phi = 0°, 30°$ and $45°$ azimuthal planes for $\triangle x/D = 0$, $\triangle y/D = .75$, $\alpha = 0°$.

Figure 17. Inviscid, laminar, and turbulent flow pressure distributions on projectile surface in the pitch plane ($\phi = 0, 180°$) for $\Delta x/D = 0$, $\Delta y/D = .75$, $\alpha = 0°$.
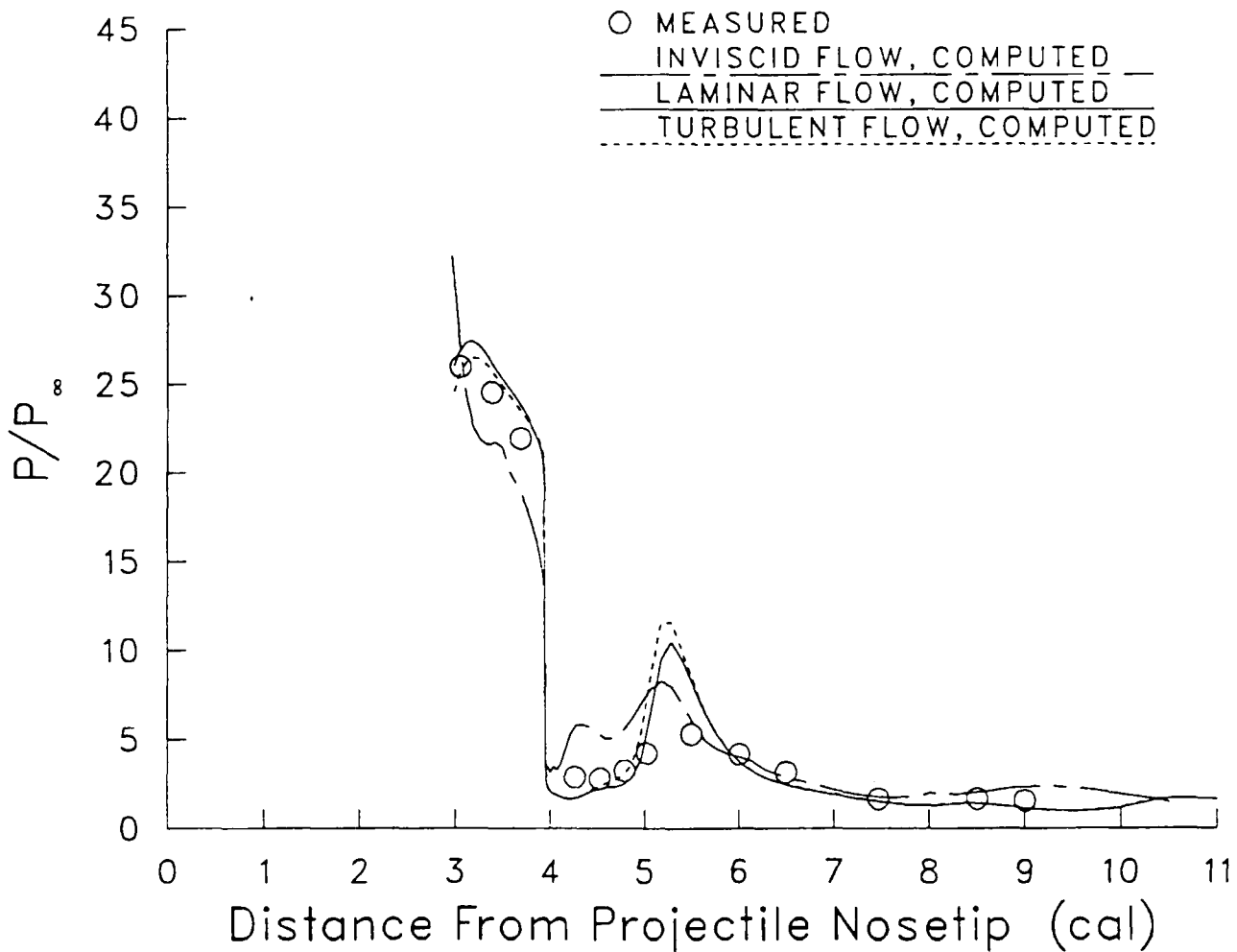
Figure 18. Inviscid, laminar, and turbulent flow pressure distributions on sabot inner surface in the pitch plane ($\phi = 0, 180°$) for $\Delta x/D = 0$, $\Delta y/D = .75$, $\alpha = 0°$.
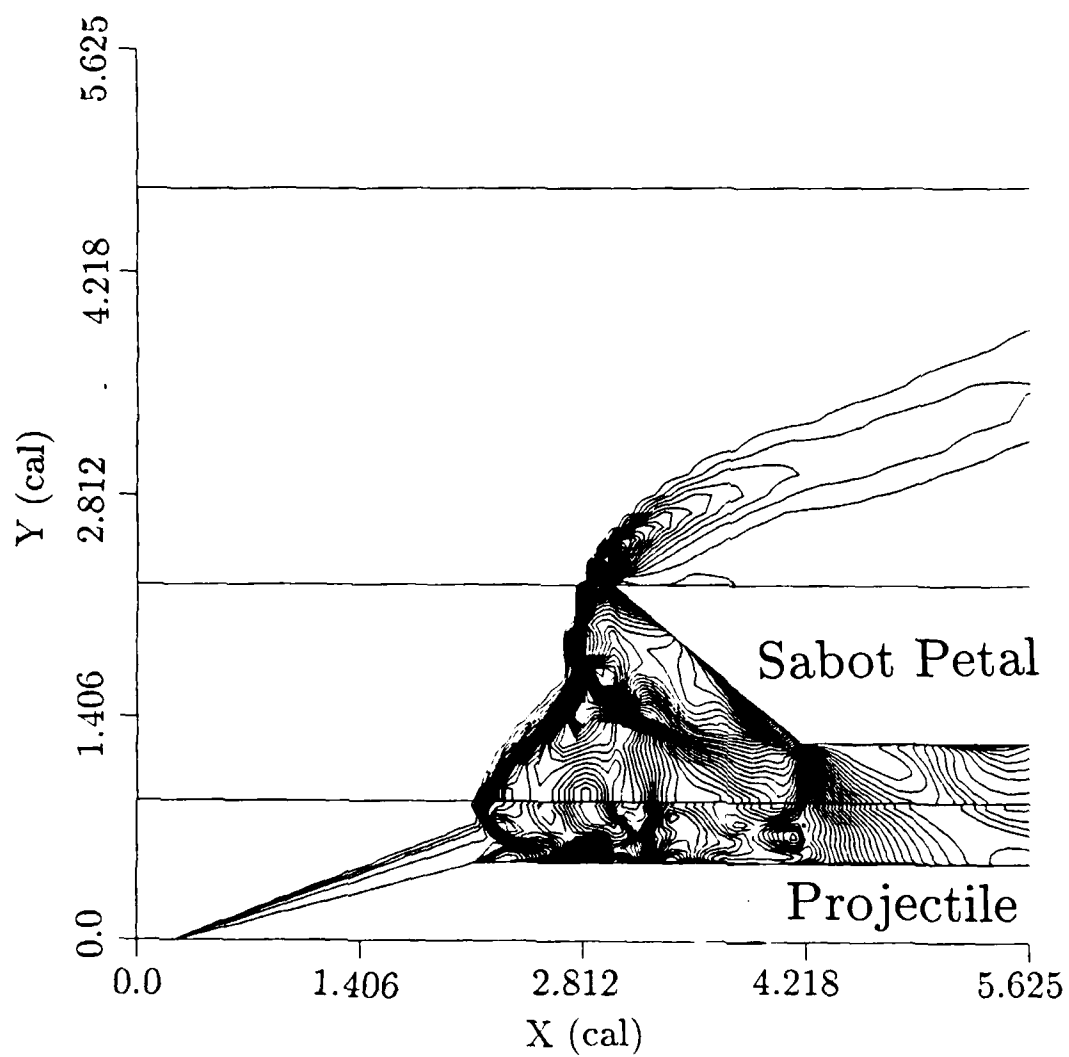
Figure 19. Laminar flow pressure contours in the pitch plane for projectile with splitter plates, $\triangle x/D = 0$, $\triangle y/D = .75$, $\alpha = 0°$.
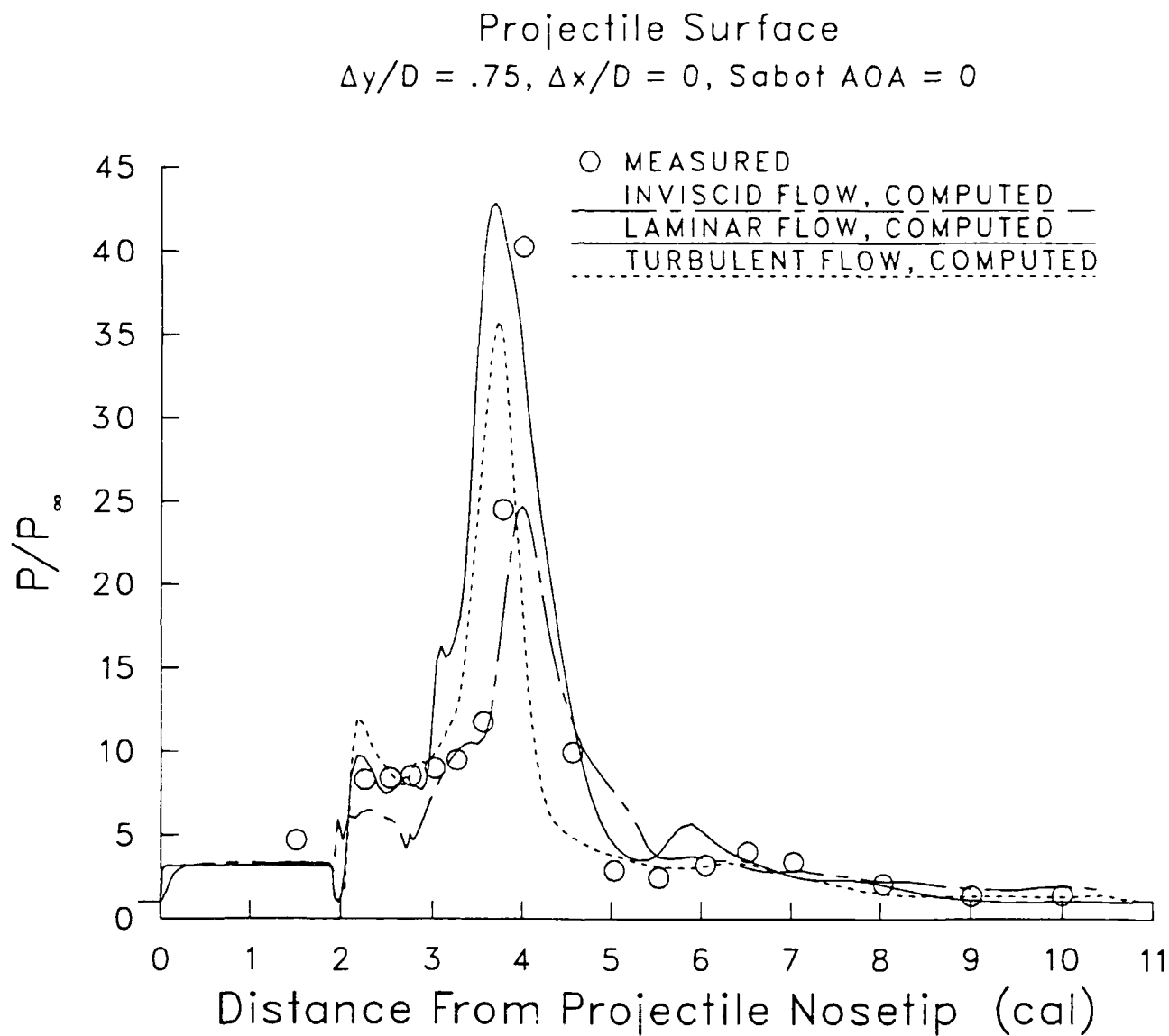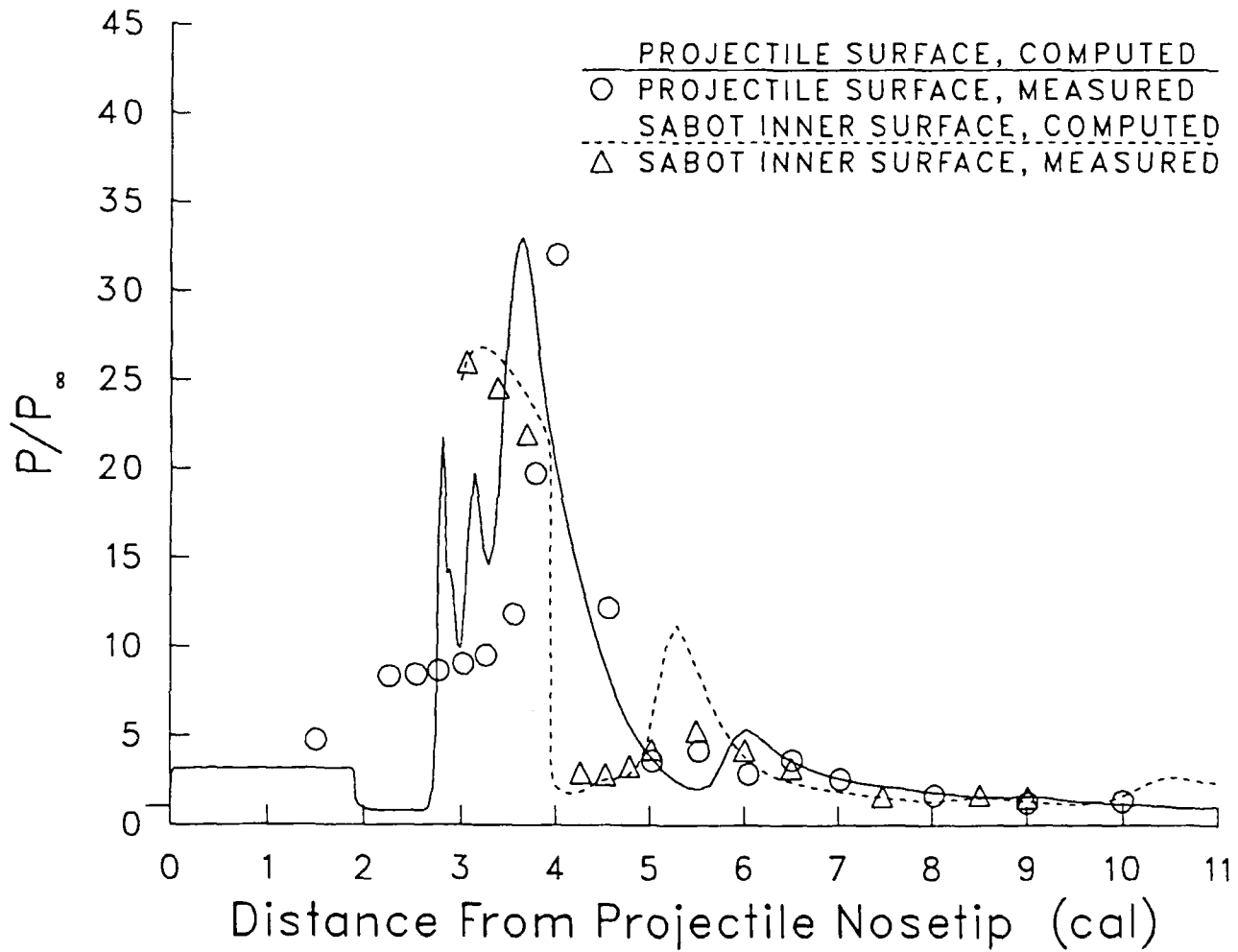
Figure 20. Laminar flow pressure distributions on projectile and sabot surfaces in the pitch plane ($\phi = 0, 180°$), projectile with splitter plates, $\Delta x/D = 0$, $\Delta y/D = .75$, $\alpha = 0°$.
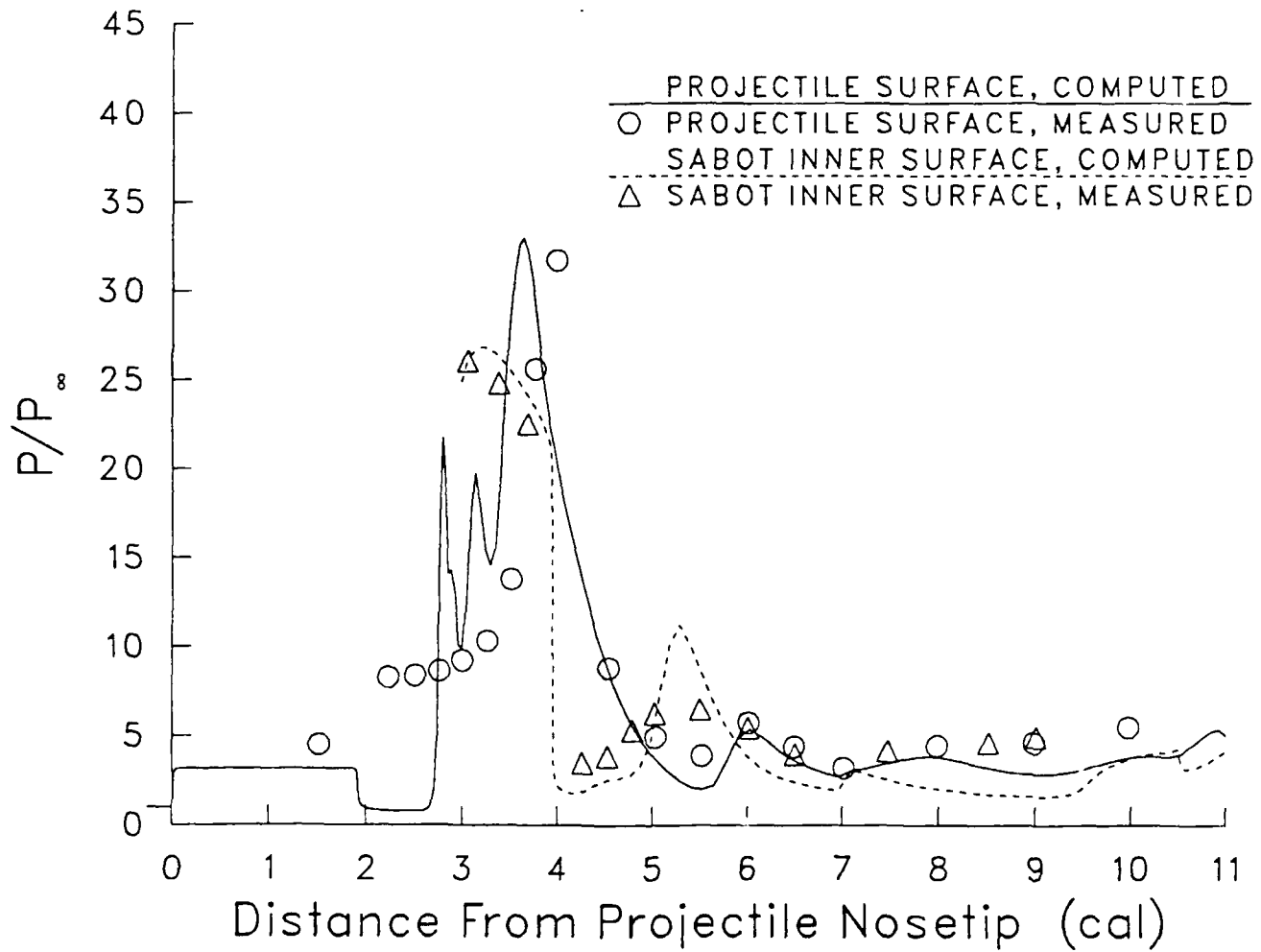
Figure 21. Laminar flow pressure distributions on projectile and sabot surfaces in the pitch plane ($\phi = 0, 180°$), projectile with splitter plates, $\triangle x/D = 0$, $\triangle y/D = .25$, $\alpha = 4°$.
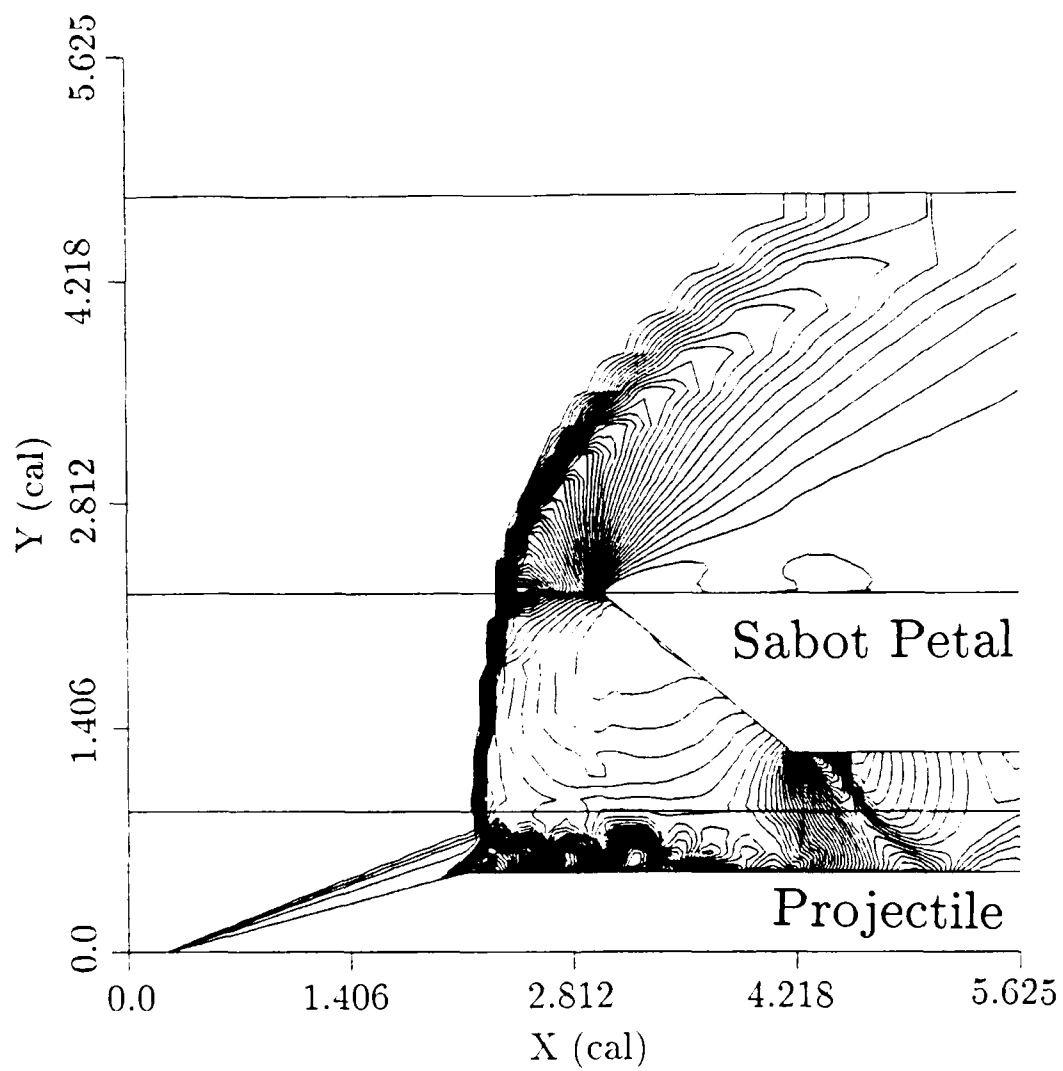
Figure 22. Laminar flow pressure contours in the pitch plane ($\phi = 0, 180°$), axisymmetric geometry, $\Delta x/D = 0$, $\Delta y/D = .75$, $\alpha = 0°$.
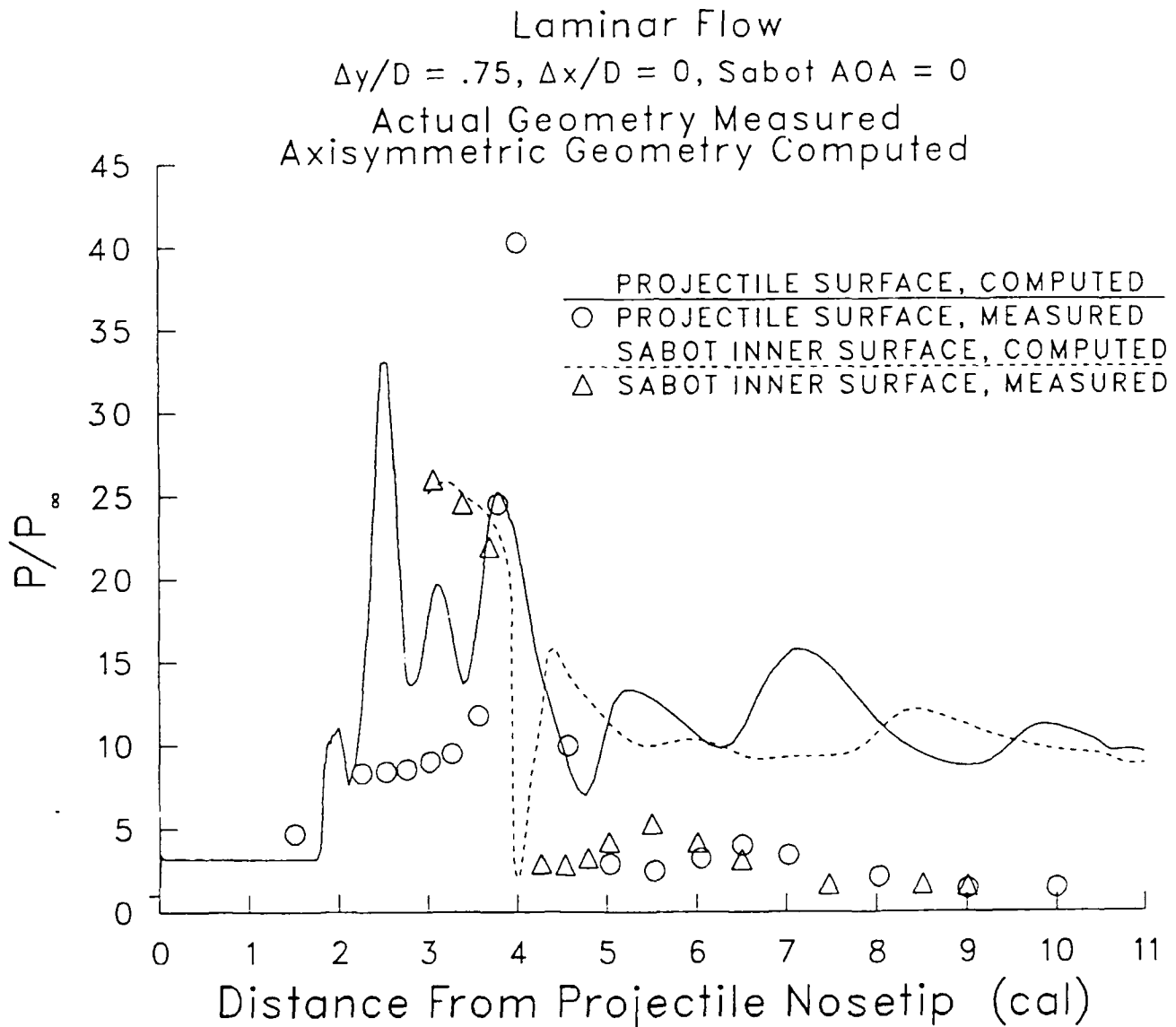
Figure 23. Laminar flow pressure distributions on projectile and sabot surfaces in the pitch plane ($\phi = 0, 180°$), axisymmetric geometry, $\Delta x/D = 0$, $\Delta y/D = .75$, $\alpha = 0°$.
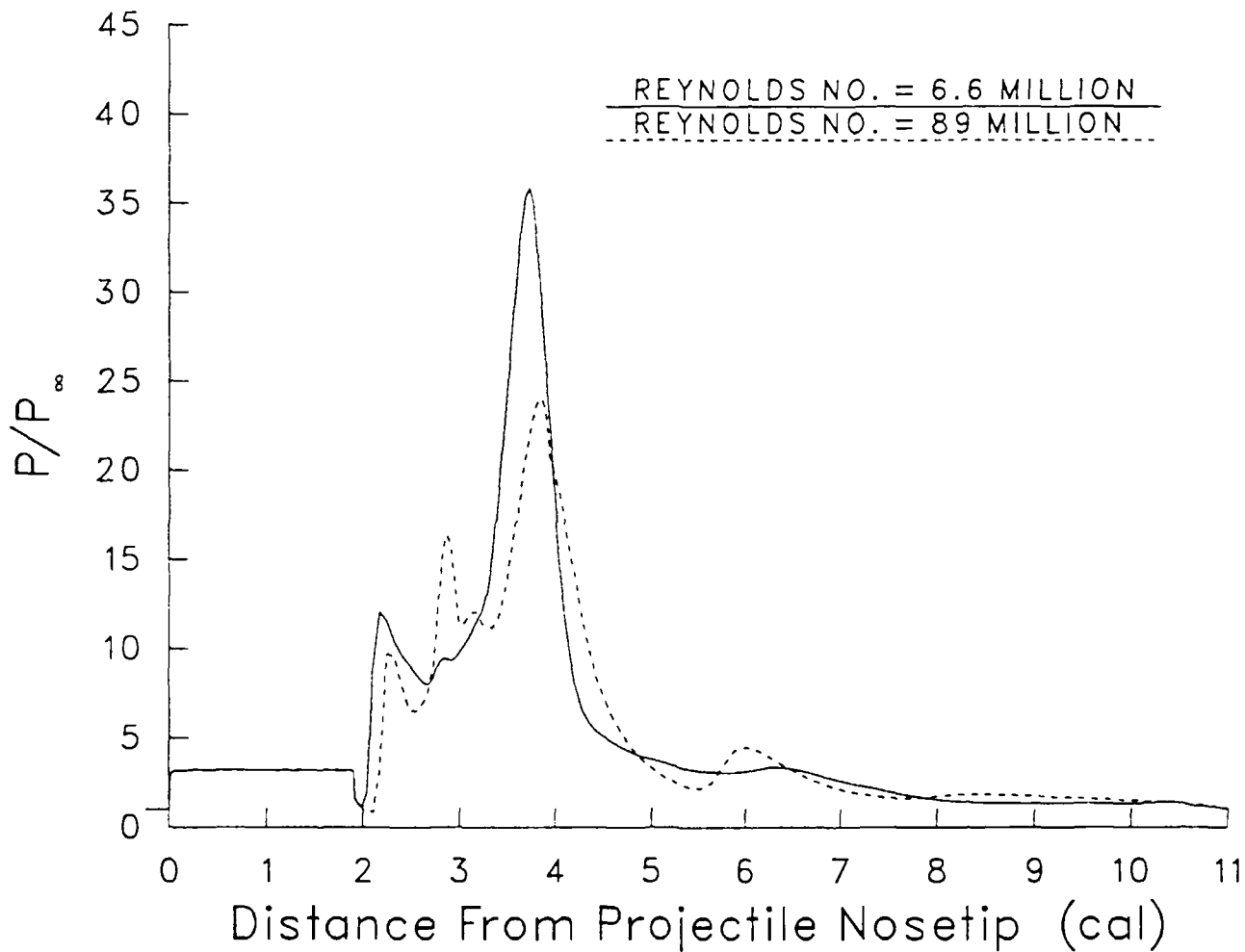
Figure 24. Turbulent flow pressure distribution on projectile surface in the pitch plane ($\phi = 0, 180°$) for $\Delta x/D = 0$, $\Delta y/D = .75$, $\alpha = 0°$. Reynolds Number 6.6 million and 89 million.

References

1. Schmidt, E.M., and Shear, D.D., "Aerodynamic Interference During Sabot Discard," AIAA Journal of Spacecraft and Rockets, Vol. 15, No. 3, May-June 1978, pp. 162-167.

2. Schmidt, E.M., and Shear, D.D., "Launch Dynamics of a Single Flechette Round," US Army Ballistic Research Laboratory, Aberdeen Proving Ground, MD, BRL Report No. 1810, Aug. 1975.

3. Schmidt, E.M., "Wind-Tunnel Measurements of Sabot-Discard Aerodynamics," AIAA Journal of Spacecraft and Rockets, Vol. 18, No. 3, May-June 1981, pp. 235-240.

4. Schmidt, E.M., and Plostins, P.,"Aerodynamics of Asymmetric Sabot Discard," US Army Ballistic Research Laboratory, Aberdeen Proving Ground, MD, ARBRL-MR-03281, June 1983.

5. Crimi, P., and Siegelman, D., "Analysis of Mechanical and Gasdynamic Loadings During Sabot Discard from Gun-Launched Projectiles," US Army Ballistic Research Laboratory, Aberdeen Proving Ground, MD, ARBRL-CR-341, June 1977.

6. Siegelman, D., Wang, J., and Crimi, P., "Computation of Sabot Discard," US Army Ballistic Research Laboratory, Aberdeen Proving Ground, MD, ARBRL-CR-505, Feb. 1983.

7. Chakravarthy S.R., Szema K.Y., Goldberg U.C., Gorski J.J., and Osher S., "Application of a New Class of High Accuracy TVD Schemes to the Navier-Stokes Equations," AIAA-85-0165, Proceedings of the 23rd AIAA Aerospace Sciences Meeting, Reno NV., January 14-17, 1985.

8. Chakravarthy S.R., Szema K.Y., and Haney, J.W., "Unified Nose-to-Tail Computational Method for Hypersonic Vehicle Applications," AIAA-88-2564, Proceedings of the 6th AIAA Applied Aerodynamics Conference, Williamsburg, VA, June 6-8, 1988.

9. Ota, D.K., Chakravarthy S.R., and Darling, J.C., "An Equilibrium Air Navier-Stokes Code for Hypersonic Flows," AIAA-88-0419, Proceedings of the 26th AIAA Aerospace Sciences Meeting, Reno NV., January 11-14, 1988.

10. Palaniswamy, S., and Chakravarthy, S.R., "Finite Rate Chemistry for USA Series Codes: Formulation and Applications," AIAA-89-0200, Proceedings of the 27th AIAA Aerospace Sciences Meeting, Reno, NV, January 9-12, 1989.

11. Baldwin, B.S. and Lomax, H., "Thin Layer Approximation and Algebraic Model for Separated Turbulent Flows," AIAA-78-257, Proceedings of the 16th AIAA Aerospace Sciences Meeting, Huntsville, AL, January 16-18, 1978.

12. Goldberg U.C., "Separated Flow Treatment with a New Turbulence Model," AIAA Journal, Vol. 24, No. 10, October 1986, pp. 1711-1713.

13. Szema, K.Y., Chakravarthy S.R., Riba, W.T., Byerly, J., and Dresser, H.S., "Multi-Zone Euler Marching Technique for Flow Over Single and Multi-Body Configurations," AIAA-87-0592, Proceedings of the 25th AIAA Aerospace Sciences Meeting, Reno NV, January 12-15, 1987.

14. Szema, K.Y., Chakravarthy S.R., Pan, D., Bihari, B.L., Riba, W.T., Akdag, V.M., and Dresser, H.S., "The Application of a Unified Marching Technique for Flow Over Complex 3-Dimensional Configurations Across the Mach Number Range," AIAA-88-0276, Proceedings of the 26th AIAA Aerospace Sciences Meeting, Reno NV, January 11-14, 1988.

15. Chen, C.L., Ramakrishnan, S., Szema, K.Y., Dresser, H.S., and Rajagopal, K., "Multi-Zonal Navier-Stokes Solutions for the Multi-Body Space Shuttle Configuration," AIAA-90-0434, Proceedings of the 28th AIAA Aerospace Sciences Meeting, Reno NV, January 8-11, 1990.

16. Nusca, M.J., Chakravarthy, S.R., and Goldberg, U.C., "Computational Fluid Dynamics Capability for the Solid-Fuel Ramjet Projectile," AIAA Journal of Propulsion and Power, Vol. 6, No. 3, May-June 1990, pp. 256-262.

17. Mazor, G., Ben-Dor, G. and Igra, O., "A Simple and Accurate Expression for the Viscosity of Nonpolar Diatomic Gases up to 10,000 K," AIAA Journal, Vol. 23, No. 4, April 1985, pp. 636-638.

18. Goldberg, U.C., "Separated Flows Calculations With A New Turbulence Model," presented at the IACM First World Congress on Computational Mechanics, Austin, TX, Sept. 1986.

19. Goldberg, U.C., "Prediction of Separated Flows With A New Turbulence Model," AIAA Journal, Vol. 26, No. 4, April 1988, pp. 405-408.

20. Rajagopal, K., Lick, W., Szema, K., Ramakrishnan, S., and Chen, C., "A Versatile Multi-Zonal Gridding Technique for Complex Geometries," AIAA-90-0011, Proceedings of the 28th AIAA Aerospace Sciences Meeting, Reno NV, January 8-11, 1990.

List of Symbols

cal	= caliber, D
c_p	= specific heat capacity, constant p
c_v	= specific heat capacity, constant volume
D	= diameter of projectile cylinder section
ϵ	= specific total internal energy
F, G, H	= flux vectors (Eq. 1)
M	= Mach number
Pr	= Prandtl number
p	= pressure
$\dot{q}$	= see Eq. 8-10
$\Re$	= specific gas constant
T	= temperature
t	= time
U	= mean streamwise velocity
u, v, w	= cartesian velocity components
W	= dependent variable vector (Eq. 1)
x, y, z	= cartesian coordinates
Δx	= axial separation between projectile and sabot bases (see Fig. 6)
Δy	= vertical separation between projectile and sabot surfaces (see Fig. 6)

Greek Symbols

α	= sabot angle of attack with respect to the projectile
γ	= ratio of specific heats, c_p/c_v
ζ	= transformed coordinate
η	= transformed coordinate
μ	= molecular viscosity
ξ	= transformed coordinate
ρ	= density
$\sigma_{xx}, \sigma_{yy}, \sigma_{zz}$	= normal stress tensors
τ	= transformed time
$\tau_{xy}, \tau_{xz}, \tau_{yz}$	= shear stress tensors
ϕ	= azimuthal angle, increasing clockwise looking downstream. Pitch plane is 0 and 180°, $\phi = 0°$ oriented with top sabot (Fig. 8)

Subscripts

t	= turbulence quantity
x, y, z	= denotes spacial components
ζ	= ζ-direction transform coefficient
η	= η-direction transform coefficient
ξ	= ξ-direction transform coefficient
∞	= freestream quantity

Intentionally left blank.

No of Copies	Organization	No of Copies	Organization
2	Administrator Defense Technical Info Center ATTN: DTIC-DDA Cameron Station Alexandria, VA 22304-6145	1	Director US Army Aviation Research and Technology Activity ATTN: SAVRT-R (Library) M/S 219-3 Ames Research Center Moffett Field, CA 94035-1000
1	HQDA (SARD-TR) WASH DC 20310-0001	1	Commander US Army Missile Command ATTN: AMSMI-RD-CS-R (DOC) Redstone Arsenal, AL 35898-5010
1	Commander US Army Materiel Command ATTN: AMCDRA-ST 5001 Eisenhower Avenue Alexandria, VA 22333-0001	1	Commander US Army Tank-Automotive Command ATTN: AMSTA-TSL (Technical Library) Warren, MI 48397-5000
1	Commander US Army Laboratory Command ATTN: AMSLC-DL Adelphi, MD 20783-1145	1	Director US Army TRADOC Analysis Command ATTN: ATRC-WSR White Sands Missile Range, NM 88002-5502
2	Commander US Army, ARDEC ATTN: SMCAR-IMI-I Picatinny Arsenal, NJ 07806-5000	(Class. only) 1	Commandant US Army Infantry School ATTN: ATSH-CD (Security Mgr.) Fort Benning, GA 31905-5660
2	Commander US Army, ARDEC ATTN: SMCAR-TDC Picatinny Arsenal, NJ 07806-5000	(Unclass. only) 1	Commandant US Army Infantry School ATTN: ATSH-CD-CSO-OR Fort Benning, GA 31905-5660
1	Director Benet Weapons Laboratory US Army, ARDEC ATTN: SMCAR-CCB-TL Watervliet, NY 12189-4050	1	Air Force Armament Laboratory ATTN: AFATL/DLODL Eglin AFB, FL 32542-5000
1	Commander US Army Armament, Munitions and Chemical Command ATTN: SMCAR-ESP-L Rock Island, IL 61299-5000		**Aberdeen Proving Ground** 2 Dir, USAMSAA ATTN: AMXSY-D AMXSY-MP, H. Cohen
1	Commander US Army Aviation Systems Command ATTN: AMSAV-DACL 4300 Goodfellow Blvd. St. Louis, MO 63120-1798	1 3 1	Cdr, USATECOM ATTN: AMSTE-TD Cdr, CRDEC, AMCCOM ATTN: SMCCR-RSP-A SMCCR-MU SMCCR-MSI Dir, VLAMO ATTN: AMSLC-VL-D

No. of
Copies Organization

No. of
Copies Organization

1 Commander
US Army, ARDEC
ATTN: SMCAR-AET-A, R. Kline
Picatinny Arsenal, NJ 07806-5000

1 Commander
Naval Surface Warfare Center
ATTN: Dr. W. Yanta,
Aerodynamics Branch
K-24, Bldg. 402-12
White Oak Laboratory
Silver Spring, MD 20910

1 Air Force Armament Laboratory
ATTN: AFATL/FXA, G.L. Winchenbach
Eglin AFB, FL 32542-5434

1 Air Force Armament Laboratory
ATTN: AFATL/FXP, C.J. Cottrell
Eglin AFB, FL 32542-5434

3 Director
NASA
Langley Research Center
ATTN: Technical Library
David H. Rudy
Jerry South
Langley Station
Hampton, VA 23365

3 Director
Sandia National Laboratories
ATTN: W. Oberkampf
F. Blottner
A. Hoddapp
Division 1636
Albuquerque, NM 87185

1 AAI Corporation
ATTN: J. Hebert
P.O. Box 126
Hunt Valley, MD 21030-0126

2 Aerojet General Corporation
ATTN: W. Wolterman
S. Rush
P.O. Box 296
Azusa, CA 91702

1 Aerospace Corporation
Aero-Engineering Subdivision
ATTN: Walter F. Reddall
El Segundo, CA 92045

2 Arrow Technology Associates, Inc.
ATTN: R. Whyte
W. Hathaway
P.O. Box 4218
South Burlington, VT 05401-0042

1 Calspan Corporation
ATTN: W. Rae
P.O. Box 400
Buffalo, NY 14225

1 Chamberlain Manufacturing Corporation
R&D Division
ATTN: W. Jones
550 Ester Street
Waterloo, IA 50704-2545

5 Honeywell, Inc.
ATTN: G. Campbell
C. Candland
D. Magnes
R. Buretta
R. Becker
7225 Northland Drive
Brooklyn Park, MN 55428

2 Olin Ordnance
ATTN: R. Taddeo
R. Davitt
10101 9th Street North
St. Petersburg, FL 33716

2 Rockwell International Science
Center
ATTN: Dr. S. Chakravarthy
Dr. K. Szema
1049 Camino Dos Rios
P.O. Box 1085
Thousand Oaks, CA 91360

No. of
Copies Organization

1 Georgia Institute of Technology
The George W. Woodruff School of
  Mechanical Engineering
ATTN: Dr. G.P. Neitzel
Atlanta, GA 30332-0405

1 Iowa State University
Aerospace Engineering Department
ATTN: John Ievalts
304 Town Engineering Building
Ames, IA 50011

1 Director
Johns Hopkins University
Applied Physics Laboratory
ATTN: Dr. Fred Billig
Johns Hopkins Road
Laurel, MD 20707

1 North Carolina State University
Mechanical and Aerospace
  Engineering Department
ATTN: F.F. DeJarnette
Raleigh, NC 27607

1 Northwestern University
Department of Engineering Science
  and Applied Mathematics
ATTN: Dr. S.H. Davis
Evanston, IL 60201

1 Renssalaer Polytechnic Institute
Department of Math Sciences
Troy, NY 12181

2 University of California - Davis
ATTN: Dr. Harry A. Dwyer
        Dr. Joseph Steger
Davis, CA 95616

1 University of Maryland
ATTN: J.D. Anderson
College Park. MD 20740

No. of
Copies Organization

Aberdeen Proving Ground

1 Director, USAMSAA
ATTN: AMXSY-RA,
        Mr. R. Scungio

3 Commander, USATECOM
ATTN: AMSTE-TE-F,
        Mr. W. Vomocil
        AMCPM-SMK-M,
        Mr. J. Callahan
        PM-SMOKE, Bldg. 324

7 Commander, CRDEC, AMCCOM
ATTN: SMCCR-MU,
        W. Dee
        C. Hughes
        F. Dagostin
        D. Bromley
        C. Jeffers
        L. Shaft
        SMCCR-RSP-A, M. Miller

39

USER EVALUATION SHEET/CHANGE OF ADDRESS

This Laboratory undertakes a continuing effort to improve the quality of the reports it publishes. Your comments/answers to the items/questions below will aid us in our efforts.

1. BRL Report Number _____ BRL-TR-3167 _____ Date of Report ____ OCTOBER 1990 ____

2. Date Report Received _____

3. Does this report satisfy a need? (Comment on purpose, related project, or other area of interest for which the report will be used.) _____

_____

_____

4. Specifically, how is the report being used? (Information source, design data, procedure, source of ideas, etc.) _____

_____

_____

5. Has the information in this report led to any quantitative savings as far as man hours or dollars saved, operating costs avoided, or efficiencies achieved, etc? If so, please elaborate. _____

_____

_____

6. General Comments. What do you think should be changed to improve future reports? (Indicate changes to organization, technical content, format, etc.) _____

_____

_____

_____

	Name _____
CURRENT ADDRESS	Organization _____
	Address _____
	City, State, Zip Code _____

7. If indicating a Change of Address or Address Correction, please provide the New or Correct Address in Block 6 above and the Old or Incorrect address below.

	Name _____
OLD ADDRESS	Organization _____
	Address _____
	City, State, Zip Code _____

(Remove this sheet, fold as indicated, staple or tape closed, and mail.)
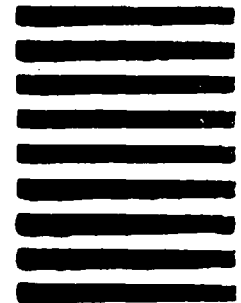
----------FOLD HERE----------

**NO POSTAGE
NECESSARY
IF MAILED
IN THE
UNITED STATES**

BUSINESS REPLY MAIL
FIRST CLASS PERMIT No 0001, APG, MD

POSTAGE WILL BE PAID BY ADDRESSEE

Director
U.S. Army Ballistic Research Laboratory
ATTN: SLCBR-DD-T
Aberdeen Proving Ground, M. 21005-9989

----------FOLD HERE----------